

STRUCTURE AND EVOLUTION OF CIRCUMBINARY DISKS AROUND SUPERMASSIVE BLACK HOLE (SMBH) BINARIES.

ROMAN R. RAFIKOV^{1,2}
Draft version July 23, 2018

ABSTRACT

It is generally believed that gaseous disks around supermassive black hole (SMBH) binaries in centers of galaxies can facilitate binary merger and give rise to observational signatures both in electromagnetic and gravitational wave domains. We explore general properties of circumbinary disks by reformulating standard equations for the viscous disk evolution in terms of the viscous angular momentum flux F_J . In steady state F_J is a linear function of the specific angular momentum, which is a generalization of (but is not equivalent to) the standard constant \dot{M} disk solution. If the torque produced by the central binary is effective at stopping gas inflow and opening a gap (or cavity) in the disk, then the inner part of the circumbinary disk can be approximated as a constant F_J disk. We compute properties of such disks in different physical regimes relevant for SMBH binaries and use these results to understand the gas-assisted evolution of SMBH pairs starting at separations $10^{-4} - 10^{-2}$ pc. We find the following. (1) Pile-up of matter at the inner edge of the disk leads to continuous increase of the torque acting on the binary and can considerably accelerate its orbital evolution compared to the gravitational wave-driven decay. (2) Torque on the binary is determined non-locally and does not in general reflect the disk properties in the vicinity of the binary. (3) Binary evolution depends on the past history of the disk evolution. (4) Eddington limit can be important in circumbinary disks at late stages of binary evolution even if they accrete at sub-Eddington rates. (5) Circumbinary disk self-consistently evolved under the action of the binary torque emits more power and has spectrum different from the spectrum of a constant \dot{M} disk — it is steeper ($\nu F_\nu \propto \nu^{12/7}$) and extends to shorter wavelength, facilitating its detection. Our results can be used for understanding properties of circumbinary disks in other astrophysical settings.

Subject headings: accretion, accretion disks — galaxies: nuclei

1. INTRODUCTION.

Physics of gaseous disks around astronomical objects, also known as accretion disks, has been one of the most important topics in astrophysics since the pioneering works of Shakura & Sunyaev (1973), Novikov & Thorne (1973), Lynden-Bell & Pringle (1974; hereafter LBP74). Historically, a lot of attention has been paid to understanding the properties of disks in which the mass accretion rate \dot{M} is constant with radius. Some other varieties of disks have been studied as well, in particular the so-called *circumbinary disks* — gaseous disks orbiting a central binary, which can be a stellar binary or a pair of supermassive black holes (SMBHs) in centers of galaxies. The latter type of systems has recently attracted a lot of attention since the tidal interaction of the SMBH binary with the disk results in the loss of the orbital angular momentum of the former and its faster inspiral. This may help resolve the so-called “last parsec” problem (Yu 2002; Lodato et al. 2009) — stalling of the SMBH binaries at separations of $10^{-3} - 1$ pc caused by the inefficiency of stellar dynamical processes at shrinking their orbits. Such circumbinary disks are the prime focus of this work.

Depending on the mass ratio of the binary components one can have different modes of tidal coupling of the binary with the disk. When the secondary-to-primary mass

ratio $q \equiv M_s/M_p$ is very small, the secondary cannot perturb the disk significantly and migrates through it in the so-called Type I migration regime familiar from the studies of protoplanetary disk-planet interaction (Ward 1997). At higher mass ratios³ the secondary becomes capable of clearing gas from the annulus around its orbit, switching its orbital evolution into the so-called Type II migration regime. As q gets closer to unity the gap around the orbit of the secondary turns into a central cavity inside of which the binary resides. Numerical simulations (MacFadyen & Milosavljević 2008; Cuadra et al. 2009) typically show that for $q \sim 1$ the size of the cavity is about twice the semi-major axis of the binary orbit.

Deposition of the angular momentum of the density waves excited by the binary causes non-trivial evolution of the circumbinary disk. The seminal study of LBP74 followed by works of e.g. Lightman & Eardley (1974), Lin & Papaloizou (1996) have shown that the behavior of disks evolving under the action of both the internal viscosity and the external torque can be described by a simple equation

$$\frac{\partial \Sigma}{\partial t} = -\frac{1}{r} \frac{\partial}{\partial r} \left[\left(\frac{\partial l}{\partial r} \right)^{-1} \frac{\partial}{\partial r} \left(r^3 \nu \Sigma \frac{\partial \Omega}{\partial r} \right) + \frac{2 \Sigma \Lambda}{\Omega} \right], \quad (1)$$

where Λ is the external torque per unit mass of the disk. Here Σ and ν are the surface density and kinematic viscosity of the disk, t and r are time and radius, and

³ The exact transition between the Type I and II regimes depends not only on q but also on the viscosity and other disk parameters, see Lin & Papaloizou (1986), Rafikov (2002).

¹ Department of Astrophysical Sciences, Princeton University, Ivy Lane, Princeton, NJ 08540; rrr@astro.princeton.edu

² Sloan Fellow

$l = \Omega(r)r^2$ is the specific angular momentum for circular orbit.

In this work, following LBP74 and Lyubarskij & Shakura (1987) we reformulate equation (1) in a more convenient form which allows a very straightforward interpretation of the steady state disk structure and provides a transparent way of understanding the evolution of circumbinary disks. This allows us to describe the structure and electromagnetic signatures of the circumbinary disks around SMBH binaries, their variation in time, and the back-reaction onto the orbital evolution of the central binary, leading to its inspiral.

Our work is structured as follows. In §2 we provide a general description of the coupled disk-binary evolution, derive governing equations, and obtain steady state solutions that generalize previously known results. In §3.1 we provide the description of the properties of disks around SMBH binaries parametrizing them via the viscous angular momentum flux rather than the mass accretion rate \dot{M} . This parametrization allows simple description of the properties of steady state circumbinary disks. In §4 we discuss evolution of circumbinary disks, in particular deriving the self-similar solutions to an evolving disk structure. All these results are then used in §5 to describe the coupled evolution of a SMBH binary and a circumbinary disk, including the self-consistent time variation of the disk properties, the orbital inspiral of the binary components, and the electromagnetic manifestations of the system. Our main results are summarized in §6.

2. PROBLEM SETUP AND EVOLUTION EQUATION.

We consider a binary consisting of two point masses M_p and $M_s < M_p$ (total mass is $M_c = M_p + M_s$), moving around common barycenter on circular orbits (for simplicity we neglect the possibility of non-zero eccentricity). Binary is surrounded by a prograde, coplanar disk (cf. Nixon et al. 2011) which extends to much larger distances than the binary semi-major axis r_b . We assume the eccentricity of the binary to be negligible, even though simulations show the possibility of eccentricity growth due to the tidal binary-disk coupling (Roedig et al. 2011).

The disk is truncated by the binary torque at the radius r_{in} ; the width of the gas-depleted annulus between the orbit of the secondary and r_{in} is $\Delta \equiv |r_{in} - r_b| \lesssim r_b$ for $q \ll 1$ while $\Delta \sim r_b$ for $q \sim 1$ (MacFadyen & Milosavljević 2008). For simplicity we assume that neither the primary nor the secondary have their own disks (this simplification can be easily relaxed). The detailed conditions for gap opening by a massive perturber in a disk can be found elsewhere (Lin & Papaloizou 1986, Rafikov 2002). Here we just assume that the binary torque clears out a clean central cavity in the disk. In practice this generally sets a lower limit on the mass ratio of the binary components q (determined by the local conditions in the disk), below which the tidal torque of the secondary is too weak to prevent viscous refilling of the gap (or cavity). We determine the conditions under which such an overflow of the disk across the orbit of the secondary (Kocsis et al. 2012a,b) is possible in §5.2.5.2.6.

External torque Λ due to tides raised by the central binary is expected to be concentrated right at the edge of the gap or cavity around the orbit of the secondary. This

expectation is borne out in calculations of the torque density distribution both in uniform disks, where it is generally found that $\Lambda \propto |r - r_b|^{-4}$ (Goldreich & Tremaine 1980; Armitage & Natarajan 2002), and in nonuniform disks, where it has been shown by Petrovich & Rafikov (2012) that Λ decays *exponentially* near the disk edge. As a result, already at small separations from r_{in} the term proportional to Λ in equation (1) can be neglected; this equation then reduces to its classical form first obtained by LBP74. Effect of the binary torque is then incorporated in the solution of this simplified equation via the boundary condition (discussed in §2.1) imposed at the inner edge of the disk.

Throughout this work we will assume the potential in which the disk orbits to be faithfully represented by a Newtonian potential produced by a combined mass M_c .

Evolution of an accretion disk is best illustrated if we characterize the disk at each radius not by its surface density Σ but by the viscous angular momentum flux F_J defined as

$$F_J \equiv -2\pi\nu\Sigma r^3 \frac{d\Omega}{dr} = 3\pi\nu\Sigma\Omega r^2, \quad (2)$$

where the last equality is for Keplerian disks with $\Omega = (GM_c/r^3)^{1/2}$. This quantity represents the viscous torque exerted by the part of the disk interior to a given radius r on the external part of the disk, and is thus equal to the amount of angular momentum crossing the disk circumference $2\pi r$ per unit time due to the action of viscosity.

In the absence of external torques mass accretion rate through the disk can be directly expressed (LBP74) through the divergence of the viscous angular momentum flux as (note that we take $\dot{M} > 0$ for mass inflow towards the center of the system)

$$\dot{M}(r) = \left(\frac{dl}{dr}\right)^{-1} \frac{\partial F_J}{\partial r} = \frac{\partial F_J}{\partial l}, \quad (3)$$

motivating us to change the independent variable from r to l . In this case the evolution equation (1) with $\Lambda = 0$ takes on a particularly simple form (LBP74; Filipov 1984; Lyubarskij & Shakura 1987):

$$\frac{\partial}{\partial t} \left(\frac{F_J}{D_J} \right) = \frac{\partial^2 F_J}{\partial l^2}, \quad (4)$$

where the function similar to the diffusion coefficient

$$D_J \equiv -\nu r^2 \frac{d\Omega}{dr} \frac{dl}{dr} \quad (5)$$

is in general a function of both l and F_J because of the possible dependence of ν on F_J .

Despite the mathematical simplicity of the evolution equation (4), which was first recognized by LBP74, over the years it has become conventional to study disk evolution using the more complicated equation (1). We show next that use of equation (4) allows certain advantages over the standard approach, in particular for obtaining the steady state solutions for the disk structure.

2.1. Boundary conditions.

Using equation (1) and continuity equation one finds

$$-\dot{M} = - \left(\frac{\partial l}{\partial r} \right)^{-1} \frac{\partial F_J}{\partial r} + 4\pi \frac{\Sigma \Lambda}{\Omega}. \quad (6)$$

As we mentioned before, Λ is expected to be significant only in a narrow annulus at the inner edge of the disk. We may then assume for simplicity that $\Lambda = 0$ outside of some radius r_Λ , which is not too different from r_{in} (to be specific, one can e.g. take r_Λ to be the radius interior to which the binary exerts 90% of its torque on the disk). Multiplying equation (6) by dl/dr and integrating between r_b and r_Λ one gets

$$F_J(r_\Lambda) = 2\pi \int_{r_b}^{r_\Lambda} r \Lambda \Sigma dr + \frac{1}{2} \int_{r_b}^{r_\Lambda} \dot{M} \Omega r dr, \quad (7)$$

where we set $F_J(r_b) = 0$ because $\Sigma(r_b) = 0$ by our assumption of a clean gap.

The first integral on the right hand side of this expression is the total torque that the binary exerts on the disk. As long as the orbital evolution of the binary is driven predominantly by the tidal coupling to the disk (and not due to the gravitational wave emission) conservation of the angular momentum ensures that this term is equal to

$$-\frac{dL_b}{dt} = -\frac{L_b}{2r_b} v_b, \quad (8)$$

where $L_b = M_c(GM_c r_b)^{1/2} q / (1+q)^2$ is the orbital angular momentum of the binary and $v_b \equiv dr_b/dt$ is its inspiral speed.

In the second integral in equation (7) one can write $\dot{M} = 2\pi \Sigma r v_r$, where v_r is the radial velocity of the gas, and approximate $v_r \sim v_b$ in the annulus between r_b and r_Λ , thus assuming that gas in this annulus closely follows the shrinkage of the binary orbit. Then one can easily see that as long as the mass of the secondary M_s satisfies the condition

$$M_s \gtrsim \frac{1}{\Omega(r_b)r_b} \int_{r_b}^{r_\Lambda} \Sigma \Omega r^2 dr, \quad (9)$$

the second term in the right hand side of equation (7) is smaller than the first one. This condition is often replaced by demanding that the ‘‘local disk mass’’ $M_d \equiv \Sigma r^2$ in the vicinity of the binary (i.e. at $r \sim r_b$) be less than the mass of the secondary (SC95, hereafter SC95; Haiman et al. 2009).

Whenever we are in the limit (9) the viscous angular momentum flux in the inner region of the disk can be directly related to the orbital evolution of the binary:

$$F_J(r_{in}) = -\frac{dL_b}{dt}. \quad (10)$$

Here we replaced r_Λ with r_{in} since the two radii are very similar (and also very close to r_b). On the contrary, if the condition (9) is not fulfilled the inner part of the disk absorbs most of the angular momentum brought in by viscous torques and equation (10) becomes invalid. In this case a more general boundary condition in the form (7) must be employed.

Using definition (2) and expression for L_b one can rewrite equation (10) as a formula for the orbital evolution time of the binary $t_{ev} = |d \ln r_b / dt|^{-1}$:

$$t_{ev} = \frac{L_b}{2F_J(r_{in})} = \frac{t_\nu}{6\pi(1+q)} \frac{M_s}{M_d}, \quad (11)$$

where we defined the viscous timescale $t_\nu \equiv r^2/\nu$, evaluated at r_b . Similar expressions (up to a constant factor) have previously been quoted in the literature on Type II migration in the limit of $M_d \ll M_s$, see e.g. Lodato et al. (2009), Baruteau & Masset (2012). A subtle point in this expression is that both t_ν and M_d vary in time as the disk evolves even if the orbit of the secondary does not change appreciably. Calculation of this evolution is one of the goals of our present work.

Previously SC95 have used equation (10) coupled with the condition $v_r \rightarrow v_b$ as $r \rightarrow r_{in}$ as a boundary condition for the problem of the circumbinary disk evolution. They have also assumed that a steady state solution for the disk structure can always be obtained even far from the binary, despite the fact that the radius r_b (at which the inner boundary condition is imposed) evolves as the secondary migrates. Because of this inconsistency their solution explicitly depends on time via the dependence on $r_b(t)$ (and the torque on the binary is found to depend on the mass of the secondary) and should evolve on the migration timescale of the secondary. However, the latter is much shorter than the viscous timescale of the disk far from the binary, where this solution is still assumed to be valid (by construction, the migration timescale of the secondary is of order the viscous timescale at $r_{in} \approx r_b$). As a result, viscous transport in the disk is unable to communicate information about the changing inner boundary condition outside the immediate vicinity of the inner edge of the disk, implying internal inconsistency of the quasi-steady solution derived in SC95. This issue has been first noted by Ivanov et al. (1999; hereafter IPP); nevertheless the SC95 solution is still being used in studies of the disk-assisted SMBH binary evolution (Haiman et al. 2009; Kocsis et al. 2011; Yunes et al. 2011).

In our work we take a different approach and specify the inner boundary condition in the form of the constraint on the mass accretion rate \dot{M} . Previously, IPP have used boundary conditions similar to ours, even though they have formulated them via the asymptotic behavior of the disk surface density Σ . For that reason many of our results coincide with their findings.

At large separations we normally take the disk to be a standard constant \dot{M} disk with the mass supply rate \dot{M}_∞ . But close to the binary, as $r \rightarrow r_{in}$, \dot{M} does not in general have to be equal to \dot{M}_∞ . If the tidal interaction with the binary presents a strong barrier for the gas inflow, then $\dot{M}(r_{in})$ is vanishingly small (Liu & Shapiro 2010). But in general tidal torques do not have to completely stop the mass inflow: in some situations (e.g. if the gap cleared out by the secondary is not deep/broad enough to present a serious obstacle to the gas inflow) a fraction of mass arriving at the inner edge of the disk can cross the orbit of the secondary and be accreted by one of the binary components (Kocsis et al. 2012a,b). Alternatively, gas can be removed from the circumbinary disk in the form of a wind, see §3.1.3.1.4, §5.2.5.2.5. To account for this possibility we generally use an inner boundary condition in the form

$$\left. \frac{\partial F_J}{\partial l} \right|_{r=r_{in}} = \dot{M}(r_{in}) = \chi \dot{M}_\infty, \quad (12)$$

see equation (3). Here $\chi \leq 1$ is assumed to be constant, allowing $\dot{M}(l_{in})$ to be less than \dot{M}_∞ . In practice the

value of $\dot{M}(r_{in})$ and χ is set by the strength of the tidal barrier (Liu & Shapiro 2010) and may vary in time as the system evolves.

Clearly, $\chi = 0$ implies no gas inflow across the orbit of the secondary, and this is the situation that we will often consider in this work. For $\chi = 1$ secondary does not present any barrier to the mass inflow and the disk structure reduces to that of a disk with constant $\dot{M} = \dot{M}_\infty$.

2.2. Steady state solution.

Equation (4) clearly admits a simple steady state solution (LBP74)

$$F_J(l) = F_{J,0} + F_{J,1}l, \quad (13)$$

where $F_{J,0}$ and $F_{J,1}$ are constants, and l is the specific angular momentum. This solution is completely independent of the detailed physics that determines the disk properties, since for any (even highly nonlinear) dependence of D_J on F_J and l the solution (13) still satisfies equation (4) in steady state.

According to equation (3) this solution implies $\dot{M} = F_{J,1}$ also being constant, which seems to suggest that equation (13) corresponds to the conventional accretion disk with constant \dot{M} . This however is not true in general.

First description of a constant \dot{M} accretion disk was provided in a seminal work of Shakura & Sunyaev (1973), who explored properties of disks affected only by the internal viscous stresses all the way to the central object. They have shown in particular that in such disks the local surface density $\Sigma(r)$ at each radius is related to the mass accretion rate via

$$\dot{M} = 3\pi\nu\Sigma, \quad (14)$$

while the energy loss per unit surface area of the disk scales as

$$\sigma T_{\text{eff}}^4(r) = \frac{3}{8\pi} \dot{M} \Omega^2. \quad (15)$$

Over the years the concept of constant \dot{M} disks has evolved to essentially imply disk properties given by equations (14) and (15). In the rest of this work we will call such disks *standard constant \dot{M} disks*.

Let us now consider a steady state solution in the form (13) with $F_{J,0} \neq 0$ and $F_{J,1} = \dot{M} = \text{const.}$ Combining equations (2) and (13) one finds

$$\dot{M} = 3\pi\nu\Sigma - F_{J,0}l^{-1}, \quad (16)$$

which reduces to (14) only when $F_{J,0} = 0$ and $F_J = \dot{M}l$, and results in a quite different expression for \dot{M} otherwise. In particular, it follows directly from (3) that it is possible to have a steady disk with $\dot{M} = 0$ as long as F_J is independent of radius. In such constant F_J disk surface density is related to F_J via

$$F_J = F_{J,0} = 3\pi\nu\Sigma(r)l, \quad (17)$$

which replaces equation (14). We explore properties of such disks in §3.

Similarly, the viscous energy dissipation rate in the disk per unit radius (and per unit time) $d\dot{E}/dr$ is given by

$$\frac{d\dot{E}}{dr} = -F_J \frac{d\Omega}{dr} = \frac{3}{2} \frac{F_J \Omega}{r}. \quad (18)$$

Since $d\dot{E}/dr = 4\pi r \sigma T_{\text{eff}}^4(r)$ we can write

$$\sigma T_{\text{eff}}^4(r) = \frac{3}{8\pi} \frac{F_J \Omega}{r^2}, \quad (19)$$

which in steady state described by the solution (13) yields

$$\sigma T_{\text{eff}}^4(r) = \frac{3}{8\pi} \left[\dot{M} \Omega^2(r) + \frac{F_{J,0} \Omega}{r^2} \right]. \quad (20)$$

Again, this expression reduces to the conventional result (15) only when $F_{J,0} = 0$. In the case of $\dot{M} = 0$ disk with $F_J = F_{J,0}$ one finds

$$T_{\text{eff}}(r) = \left(\frac{3}{8\pi} \frac{F_J \sqrt{GM_c}}{\sigma} \right)^{1/4} r^{-7/8}, \quad (21)$$

so that $T_{\text{eff}}(r)$ increases towards small radii more steeply than in a standard constant \dot{M} disk (for which $T_{\text{eff}}(r) \propto r^{-3/4}$). This result was first obtained by SC95.

Equation (19) predicts non-zero T_{eff} for a disk with $F_J = \text{const.}$, even though $\dot{M} = 0$ in such a disk. Since there is no inward mass flow in this disk and corresponding release of potential energy is absent one may naturally wonder where does the energy emitted from the disk surface come from. Integrating equation (18) between arbitrarily chosen inner and outer radii r_i and r_o one finds the global energy release between these radii

$$\dot{E}(r_i < r < r_o) = F_J [\Omega(r_i) - \Omega(r_o)], \quad (22)$$

where we have used the fact that F_J is independent of r . Thus, the global rate of energy generation by viscous dissipation is equal to the work done on the disk by the viscous stress at its inner and outer edges. The latter ultimately provides the energy source for the radiation from the disk surface.

To summarize, the assumption of a steady state does not necessarily require \dot{M} and T_{eff} in a disk to be given by standard equations (14) and (15) — these equations are sufficient but not necessary characteristics of steady disks. The most general steady state is in fact described by equation (13) and then it follows that \dot{M} and T_{eff} must be given by equations (16) and (20). In the rest of the paper we explore the properties of such “non-standard” disks.

3. DISK PROPERTIES AS A FUNCTION OF F_J .

It is conventional to describe the structure of steady state accretion disks using the mass accretion rate \dot{M} , assumed to be constant with radius, as a free parameter (e.g. Shakura & Sunyaev 1973). Such calculations universally assume that relations (14) and (15) hold true, i.e. that $F_{J,0} = 0$ in equation (13). Having shown in §2.2.2 that in general steady state does not require $F_{J,0} = 0$ we now revise these scalings by expressing disk properties in terms of F_J , which may in general be a function of both time and radius r or specific angular momentum l , rather than \dot{M} . When an additional assumption $F_J = \text{const.}$ is made these relations naturally describe the properties of $\dot{M} = 0$ disks, see §2.2.2.

In our calculations we will always make an assumption of an optically thick disk, but it is easy to extend them to optically thin disks as well. Because of the large range of

radii spanned by disks in some systems, the conditions in them are expected to vary with radius, resulting in transitions in the opacity behavior. To account for this in Appendix A we derive a set of scaling relations applicable to the gas pressure dominated disks with power law opacity behavior, and apply them in §3.1 to disks around SMBH binaries.

3.1. Circumbinary disks around SMBH binaries.

Structure of the inner region of a circumbinary disk around a SMBH binary may be strongly affected by the radiation pressure. We parametrize its role by a dimensionless ratio of the gas pressure to total pressure $\beta \equiv p_g/p = p_g/(p_r + p_g)$, where $p_g = \rho kT/\mu$ is the gas pressure and $p_r = aT^4/3$ is the radiation pressure. In the radiation pressure dominated case $\beta \ll 1$, while in the gas pressure dominated case $1 - \beta \ll 1$.

Behavior of viscosity in the radiation pressure dominated fluid is not well understood at the moment. There is still an ongoing debate whether it is determined by the full pressure or just the gas pressure in the disk. For that reason we use a prescription motivated by the conventional α -parametrization of Shakura & Sunyaev (1973) and accounting for the two possibilities in a convenient form (Goodman 2003):

$$\nu = \alpha \beta^b \frac{c_s^2}{\Omega}. \quad (23)$$

Here $b = 0$ corresponds to kinematic viscosity proportional to the full pressure p , while $b = 1$ corresponds to the case when only the gas pressure p_g determines the viscosity. Lightman & Eardley (1974) suggested that radiation pressure dominated disks with $b = 0$ are thermally unstable but recent numerical work by Hirose et al. (2009a,b) does not show this to be the case.

Disks around SMBH binaries are heated by internal viscous dissipation and also by energy deposition of the density waves launched by the central binary. For simplicity we do not consider here the latter contribution (its role has been studied by Lodato et al. 2009) and assume that disk heating is described by equations (18) and (19). Using equation (21) we estimate the effective temperature of the disk as

$$T_{\text{eff}}(r) = \left(\frac{3}{8\pi} \frac{F_J \sqrt{GM_c}}{\sigma} \right)^{1/4} r^{-7/8} \quad (24)$$

$$\approx 1.1 \times 10^3 \text{K} F_{J,50}^{1/4} M_{c,7}^{1/8} r_{-2}^{-7/8},$$

where $M_{c,n} \equiv M_c/(10^n M_\odot)$, $r_n \equiv r/(10^n \text{pc})$, and $F_{J,n} \equiv F_J/(10^n \text{erg})$. This estimate assumes a particular value of F_J , which we motivate in §3.1.3.1.4.

In our treatment of the vertical radiation transfer in the disk we follow Goodman (2003) and relate the mid-plane disk temperature T to T_{eff} via

$$T^4 = \frac{\tau}{2} T_{\text{eff}}^4, \quad (25)$$

typical for optically thick ($\tau \gg 1$) disks, where $\tau = \kappa \Sigma$ is the optical depth. Also,

$$\Sigma = 2\rho h, \quad (26)$$

where ρ is the characteristic disk density, $h = c_s/\Omega$ is the disk scale height and $c_s = (p/\rho)^{1/2}$ is the sound speed,

determined by the total pressure p . In the innermost region of the disk where the transition between the radiation and gas pressure dominated regimes occurs we assume opacity to be dominated by electron scattering, i.e. $\kappa = \kappa_{es} \approx 0.4 \text{ cm}^2 \text{ g}^{-1}$. Further out, in the gas pressure dominated part of the disk, κ is determined by the free-free opacity. We separately consider all these regimes below.

Combining equations (2), (19), (23), (25), & (26) one finds the following equation determining the value of β for a disk with opacity dominated by electron scattering:

$$\frac{\beta^{4+b}}{(1-\beta)^{10}} = 2^6 \pi^8 \left(\frac{k}{\mu} \right)^4 \frac{c^{10}}{\kappa_{es}^9 \sigma} \frac{(GM_c)^{1/2}}{\alpha F_J^8} r^{29/2}. \quad (27)$$

From that one can find the distance $r^{\text{rad/gas}}$ of the transition between the radiation and gas pressure dominated regimes by setting $\beta = 1/2$ in equation (27):

$$r^{\text{rad/gas}} = \left[\frac{2^b}{\pi^8} \alpha \left(\frac{\mu}{k} \right)^4 \frac{\kappa_{es}^9 \sigma}{c^{10}} \frac{F_J^8}{(GM_c)^{1/2}} \right]^{2/29} \quad (28)$$

$$\approx 3.8 \times 10^{-3} \text{pc} \left[2^b \frac{\alpha_{-1} \mu_{0.5}^4 F_{J,50}^8}{M_{c,7}^{1/2}} \right]^{2/29},$$

where $\alpha_n \equiv \alpha/10^n$, $\mu_n \equiv nm_p$, i.e. μ in this formula is normalized by the molecular weight of fully ionized H. Note the extremely weak dependence of $r^{\text{rad/gas}}$ on the binary mass M_c .

3.1.1. Radiation pressure dominated regime.

Interior to $r^{\text{rad/gas}}$ disk is radiation pressure dominated and by assumption $\kappa = \kappa_{es}$. In this case one finds

$$\frac{h(r)}{r} = \frac{1}{2\pi} \frac{\kappa_{es}}{c(1-\beta)} \frac{F_J}{\Omega r^3} \quad (29)$$

$$\approx 1.1 \times 10^{-3} F_{J,50} M_{c,7}^{-1/2} r_{-2}^{-3/2},$$

irrespective of the value of b in equation (23). At the same time the scalings of $\Sigma(r)$ and $T(r)$ explicitly depend on the viscosity behavior: for $b = 0$

$$\Sigma(r) = \frac{4\pi}{3} \frac{c^2}{\alpha \kappa_{es}^2 F_J} r^2 \quad (30)$$

$$\approx 2.1 \times 10^6 \text{g cm}^{-2} \alpha_{-1}^{-1} F_{J,50}^{-1} r_{-2}^2,$$

$$T(r) = \left[\frac{(GM_c)^{1/2} c^2}{4\alpha \sigma \kappa_{es}} \right]^{1/4} r^{-3/8} \quad (31)$$

$$\approx 2.9 \times 10^4 \text{K} \alpha_{-1}^{-1/4} M_{c,7}^{1/8} r_{-2}^{-3/8},$$

while for $b = 1$

$$\Sigma(r) = \left[\frac{2^4}{3^5 \pi^3} \left(\frac{\mu}{\alpha k} \right)^4 \frac{\sigma F_J^3}{(GM_c)^{1/2} \kappa_{es}} \right]^{1/5} r^{-9/10} \quad (32)$$

$$\approx 6 \times 10^4 \text{g cm}^{-2} \left[\frac{\mu_{0.5}^4 F_{J,50}^3}{\alpha_{-1}^4 M_{c,7}^{1/2}} \right]^{1/5} r_{-2}^{-9/10}$$

$$T(r) = \left[\frac{1}{2^4 \pi^2} \frac{\mu (GM_c)^{1/2} \kappa_{es}}{\alpha \sigma} F_J^2 \right]^{1/5} r^{-11/10} \quad (33)$$

$$\approx 1.2 \times 10^4 \text{K} \left[\frac{\mu_{0.5} M_{c,7}^{1/2} F_{J,50}^2}{\alpha_{-1}} \right]^{1/5} r_{-2}^{-11/10}.$$

Note that a radiation pressure dominated disk with $F_J = \text{const}$ (and $\dot{M} = 0$) has $h(r) \propto r^{-1/2}$ (as opposed to the case of a conventional $\dot{M} = \text{const}$ disk for which $h(r) = \text{const}$), i.e. the disk *puffs up* as r decreases. Surface density shows dramatically different behavior depending on the value of b : it rises with r when viscosity is proportional to the total pressure ($b = 0$), but drops with r when ν scales with the gas pressure. Finally, $T(r)$ is independent of F_J when $b = 0$ but scales as $\propto F_J^{2/5}$ for $b = 1$.

3.1.2. Gas pressure dominated regime with $\kappa = \kappa_{es}$.

Outside of $r^{\text{rad/gas}}$ gas pressure dominates, meaning that $\beta \rightarrow 1$ and $\nu \rightarrow \alpha c_s^2 / \Omega$, but initially opacity is still determined by electron scattering, so that $\kappa = \kappa_{es}$. It is easy to see that in this case the midplane temperature and surface density runs in the disk should be the same as in the radiation pressure dominated case with $b = 1$: derivation of $T(r)$ and $\Sigma(r)$ involves only the equation of vertical radiation transfer (25) and the definition (2), which are identical in two cases because the viscosity and opacity are the same when $b = 1$. Thus, the behavior of $\Sigma(r)$ and $T(r)$ in the gas pressure dominated case with $\kappa = \kappa_{es}$ is given by equations (32) and (33) correspondingly.

However, the scaling of the aspect ratio of the disk with r is different from h/r given by equation (29) since unlike the case studied in §3.1.1 the vertical support is now provided by the gas pressure. As a result one finds

$$\frac{h(r)}{r} = \left[\frac{1}{16\pi^2} \left(\frac{k}{\mu} \right)^4 \frac{\kappa_{es} F_J^2}{\alpha \sigma (GM_c)^{9/2}} \right]^{1/10} r^{-1/20} \quad (34)$$

$$\approx 6.6 \times 10^{-3} \left[\frac{F_{J,50}^2}{\alpha_{-1} \mu_{0.5}^4 M_{c,7}^{9/2}} \right]^{1/10} r^{-1/20}.$$

Note that h/r goes down with r meaning that the disk is not flared. However, this dependence on r is so weak that the aspect ratio is essentially constant with radius.

3.1.3. Gas pressure dominated regime with $\kappa = \kappa_{ff}$.

At even larger distances opacity in the disk is dominated by the free-free opacity $\kappa_{ff} = \kappa_{ff,0} \rho T^{-7/2}$, with $\kappa_{ff,0} = 8 \times 10^{22} \text{ cm}^{-1} \text{ g}^{-2} \text{ K}^{7/2}$. Using equations (32) applicable for the situation described in §3.1.2 and the behavior of the midplane temperature inferred from equation (34) one finds the transition between the two opacity regimes to take place at

$$r^{\text{es/ff}} = \left(\frac{3 \kappa_{es}^2 F_J}{8\pi \kappa_{ff,0} \sigma} \right)^{1/2} \left(\frac{k}{\mu} \right)^{1/4} \quad (35)$$

$$\approx 8.4 \times 10^{-3} \text{ pc } F_{J,50}^{1/2} \mu_{0.5}^{-1/4}.$$

Outside this radius parameters of the disk scale as

$$\Sigma(r) = \left[\frac{2^{10}}{3^{18} \pi^{14}} \left(\frac{\sigma}{\kappa_{ff,0}} \right)^2 \left(\frac{\mu}{k} \right)^{15} \frac{F_J^{14}}{\alpha^{16} (GM_c)^2} \right]^{1/20} \quad (36)$$

$$\times r^{-11/10} \approx 7.2 \times 10^4 \text{ g cm}^{-2} \frac{\mu_{0.5}^{3/4} F_{J,50}^{7/10}}{\alpha_{-1}^{4/5} M_{c,7}^{1/10}} r^{-11/10},$$

$$T(r) = \left[\frac{2^{-5} \kappa_{ff,0}}{3\pi^3 \sigma} \left(\frac{\mu}{k} \right)^{5/2} \frac{F_J^3 (GM_c)}{\alpha^2} \right]^{1/10} r^{-9/10}, \quad (37)$$

$$\approx 10^4 \text{ K } \frac{\mu_{0.5}^{1/4} F_{J,50}^{3/10} M_{c,7}^{1/10}}{\alpha_{-1}^{1/5}} r^{-9/10},$$

$$\frac{h(r)}{r} = \left[\frac{2^{-5} \kappa_{ff,0}}{3\pi^3 \sigma} \left(\frac{k}{\mu} \right)^{15/2} \frac{F_J^3}{\alpha^2 (GM_c)^9} \right]^{1/20} r^{1/20}, \quad (38)$$

$$\approx 6 \times 10^{-3} \frac{F_{J,50}^{3/10}}{\alpha_{-1}^{1/5} \mu_{0.5}^{3/4} M_{c,7}^{9/10}} r^{1/20},$$

see equations (A2)-(A4) in Appendix A. In this opacity regime disk is only weakly flared and h/r is essentially constant with radius.

3.1.4. Characteristic values of F_J .

We now try to motivate the characteristic values of the viscous angular momentum flux in disks around SMBH binaries using different arguments. In the case of constant \dot{M} disks a standard way of providing the characteristic value of \dot{M} is through the Eddington mass accretion rate

$$\dot{M}_{\text{Edd}} = \frac{4\pi GM_c}{c\kappa_{es}} \varepsilon^{-1} \approx 0.2 M_\odot \text{ yr}^{-1} \frac{M_{c,7}}{\varepsilon_{0.1}}, \quad (39)$$

where $\varepsilon = 0.1\varepsilon_{0.1}$ is the radiative efficiency.

In the case of constant F_J (or $\dot{M} = 0$) disk one can also formulate the Eddington limit on the value of F_J , which is reached when $h/r \sim 1$. When this happens radiation pressure puffs up the disk to such extent that it becomes geometrically thick. Further increase of F_J should result in mass loss caused by the radiation pressure driven wind. Another possibility for $h/r \sim 1$ is the mass overflow across the orbit of the secondary which may become possible since high above the midplane the potential of the secondary is weaker, potentially allowing the gas to cross the orbit of the secondary high above the disk midplane⁴. Both these processes result in mass loss for the circumbinary disk at its inner edge, which can have important implications for the orbital evolution of the central binary as we demonstrate in §4.

Unlike the situation with \dot{M}_{Edd} in conventional constant \dot{M} disks, the Eddington limit on F_J found from the condition $h/r = 1$ depends on the value of r at which it is evaluated, see equation (29):

$$F_{J,\text{Edd}}(r) = 2\pi \frac{(GM_c)^{1/2} c}{\kappa_{es}} r^{3/2}. \quad (40)$$

It is clear that this condition is most constraining at the inner edge of the disk $r_{in} \sim r_b$, where r_b is the semi-major axis of the SMBH binary.

Obviously, one needs to invoke additional considerations to pick a particular value of r_{in} (or r_b) at which $F_{J,\text{Edd}}$ is to be evaluated. Here we assume that this critical value of r_{in} is such that at $r_b \approx r_{in}$ the orbital decay timescale of the binary due to emission of gravitational waves t_{GW} is equal to the characteristic timescale on which the orbit of the binary shrinks due to the tidal

⁴ For $q \ll 1$ puffing up of the disk may cause the overflow of the secondary orbit even when $h/r \lesssim 1$.

coupling to the circumbinary disk t_J . The logic behind choosing this condition is that the disk then stays sub-Eddington all the way until the point when the GW emission becomes more important for the orbital evolution of the binary than its tidal coupling to the disk. Beyond this point the disk becomes super-Eddington and starts losing mass in a radiation pressure driven wind, reducing the disk torque. However this does not affect the binary inspiral since the orbital evolution is no longer sensitive to the tidal torque.

Equating

$$t_{\text{GW}}(r_b) = \frac{5}{2q_S} \frac{R_S}{c} \left(\frac{r_b}{R_S} \right)^4 \quad (41)$$

(here $q_S \equiv 4q/(1+q)^2$ and $R_S \equiv 2GM_c/c^2$ is the Schwarzschild radius of the black hole with the mass equal to the total mass of the binary M_c) and

$$t_J(r_b) = \left| \frac{d \ln r_b}{dt} \right|^{-1} = \frac{L_b}{2F_J} = \frac{q_S}{8} \frac{M_c \sqrt{GM_c r_b}}{F_J} \quad (42)$$

(here $L_b = (q_S/4)M_c(GM_c r_b)^{1/2}$ is the total orbital angular momentum of the binary) one finds

$$r_{in} = R_S \left(\frac{q_S^2}{2^{5/2} 5} \frac{M_c c^2}{F_J} \right)^{2/7}. \quad (43)$$

Plugging this value of r_{in} into equation (40) one finds that the Eddington value of the viscous angular momentum flux in $\dot{M} = 0$ disk based on the condition $t_{\text{GW}}(r_{in}) = t_J(r_{in})$ is given by

$$F_{J,\text{Edd}} = \left[\frac{2^{10} 3^3 \pi^7 (GM_c)^{14} M_c^3 q_S^6}{5^3 c^8 \kappa_{es}^7} \right]^{1/10} \quad (44)$$

$$\approx 10^{51} \text{erg} M_{c,7}^{17/10} q_S^{3/5}. \quad (45)$$

This argument justifies the adoption of a characteristic value of $F_J = 10^{50}$ erg (corresponds to $M_c = 10^7 M_\odot$, $q = 0.005$) in our numerical estimates.

One can come up with other ways of choosing critical r_{in} or the characteristic value of F_J . In particular, one may demand the disk to stay sub-Eddington until the point when t_{GW} becomes equal to the viscous timescale at r_{in} , after which the binary orbit shrinks faster than the viscosity can refill the central cavity (Milosavljević & Phinney 2005). This happens at considerably smaller value of r_{in} than that given by (43) and implies lower F_J . However, (1) at this point tidal torque is already completely negligible compared to the angular momentum loss due to the GW radiation, and (2) such condition would depend on the poorly understood value of b in equation (23). Thus, we avoid this way of constructing Eddington limit-based estimate of F_J .

One can also evaluate F_J based on arguments completely independent of the Eddington limit. For example, one may demand the value of t_{GW} at r_{in} given by (43) to be equal to some characteristic time t . This would imply that after the GW emission becomes the dominant cause of the binary inspiral, the lifetime of the binary until merger is equal to t . Such estimate gives

$$F_{J,t} = M_c c^2 \frac{q_S^{9/8}}{2^{27/8} 5^{1/8}} \left(\frac{R_S}{ct} \right)^{7/8} \quad (46)$$

$$\approx 4 \times 10^{46} \text{erg} q_S^{9/8} M_{c,7}^{15/8} \left(\frac{t}{10^{10} \text{yr}} \right)^{-7/8}.$$

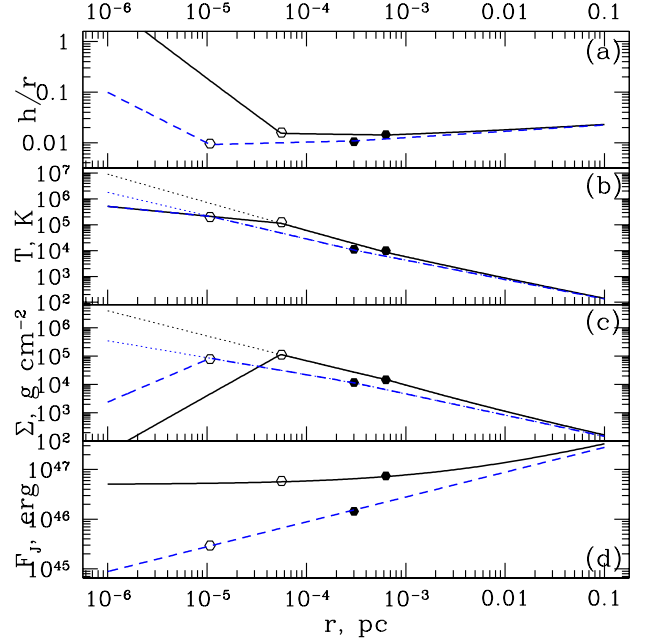


FIG. 1.— Properties of a steady disk around a SMBH binary with mass $M_c = 10^5 M_\odot$ described by a solution (13) with $F_{J,0} = 5 \times 10^{46}$ erg and mass accretion rate at infinity $F_{J,1} = \dot{M}_\infty = \dot{M}_{\text{Edd}}$ (radiative efficiency of 0.1 is assumed). Solid (black) curves describe the run of (a) aspect ratio h/r , (b) temperature T , (c) surface density Σ , and (d) angular momentum flux F_J with r in radiation pressure dominated part of the disk. Dashed (blue) curves describe the same but for a standard constant \dot{M} disk with the same mass accretion rate \dot{M}_∞ . Dotted extensions of these curves at small r correspond to $b = 1$ in radiation pressure dominated part of the disk. Open dots on each curve correspond to the transition between the radiation and gas pressure dominated regimes, while filled dots describe the transition between the electron scattering and free-free opacity.

It sets a lower limit on the value of F_J necessary for equal mass ($q_S = 1$) $M_c = 10^7 M_\odot$ SMBH binary to merge within the Hubble time. For $F_J = F_{J,\text{Edd}}$ such a binary would merge within 4×10^5 yr after the GW emission starts to dominate its orbital evolution.

Finally, using equations (2) and (23) one can also express F_J via the disk mass enclosed between its inner edge and some outer radius r_o via

$$M_{\text{disk}} = \frac{2F_J}{3\alpha} \int_{r_{in}}^{r_o} \frac{dr}{rc_s^2} \sim \frac{F_J}{\alpha c_s^2(r_o)}, \quad (47)$$

where it is assumed that gas pressure dominates (or $b = 1$), $c_s = (kT/\mu)^{1/2}$ and $F_J = \text{const}$ between r_{in} and r_o . The approximate relation in this formula is valid for $r_o \gg r_{in}$, provided that the outer regions of the disk dominate its mass — a rather natural assumption as long as the midplane temperature falls with increasing radius, as this equation shows. Note that M_{disk} explicitly depends only on the disk temperature at the outer radius but not r_o itself.

Despite the estimates (46) and (47) which have clear physical meaning, we still advocate the use of $F_{J,\text{Edd}}$ as it represents an important upper limit on F_J : for $F_J \lesssim F_{J,\text{Edd}}$ the orbital evolution of the binary is essentially not affected by the Eddington limit (even though

at late stages of inspiral the inner part of the disk may become super-Eddington and be depleted by the radiation pressure driven wind, see §5.2.5.2.5).

3.1.5. Global properties of steady state disks.

Results of §§3.1.3.1.1-3.1.3.1.3 allow us to understand global characteristics of steady circumbinary disks described by the solution (13).

In Figure 1 we demonstrate how the main properties of such a disk vary as a function of r across regions with different opacity and pressure behavior. We consider a $M_c = 10^5 M_\odot$ SMBH binary orbited by a disk described by the relation (13) with $F_{J,0} = 5 \times 10^{46}$ erg and $F_{J,1} = \dot{M}_\infty = \dot{M}_{\text{Edd}}$. Far from the binary (at $r \rightarrow \infty$) disk transitions to a standard constant $\dot{M} = \dot{M}_\infty$ accretion disk, while at small separations corresponding to $l \lesssim F_{J,0}/\dot{M}_\infty$ it becomes a constant F_J disk. Note that $\dot{M} = \dot{M}_\infty$ at all radii meaning that mass has to be removed at r_{in} at the same rate with which it is supplied at large radii.

We compare the properties of this disk to a standard constant $\dot{M} = \dot{M}_\infty$ disk in which $F_{J,0} = 0$ (dashed curves). We find that the midplane temperature T is higher in a disk with non-zero $F_{J,0}$ in all regimes. As a result, this disk is more extended vertically and becomes geometrically thick ($h/r \sim 1$) at $r = 3 \times 10^{-6}$ pc ($\approx 300 R_S$) in the radiation pressure dominated regime. Unless the disk is truncated on the inside by the binary torque at larger separation, it would presumably be losing mass at this point. Another consequence of higher T is that all transitions between different regimes occur at larger r (typically by a factor of several) in the disk with non-zero $F_{J,0}$. In particular, radiation pressure starts to dominate in this disk at $\approx 5 \times 10^{-5}$ pc as opposed to $\approx 10^{-5}$ pc in the $F_{J,0} = 0$ disk.

The comparison of the surface density structure between the two disks depends on whether $b = 1$ or 0 in the radiation pressure dominated regime. In the former case Σ keeps increasing towards small r in both types of disks, which reflects the inefficiency of viscosity proportional to (relatively small) gas pressure in the $b = 1$ case. We find Σ to be higher in the $F_{J,0} \neq 0$ disk by an order of magnitude in the radiation pressure dominated regime.

In the case of ν scaling with the radiation pressure ($b = 0$) the behavior of Σ is completely different as it falls towards small r , because of rapid increase of T and ν in the radiation pressure dominated regime. As a result, close to the binary surface density is much smaller (by more than an order of magnitude) in the disk with non-zero $F_{J,0}$. The relatively small amount of mass residing in the vicinity of the SMBH binary in this case may have implications for the properties of the afterglow following the binary merger.

It is well known (Goodman 2003) that the outer parts of disks around SMBHs may be subject to gravitational instability (Safronov 1960; Toomre 1964; Goldreich & Lynden-Bell 1965) when the Toomre Q parameter defined as $Q = \Omega c_s / (\pi G \Sigma)$ drops below unity. In the case of constant F_J disks or steady disks with $F_J(l)$ given by the solution (13) one can easily determine the radius r^{sg} at which the disk becomes self-gravitating using our results for $T(r)$ and $\Sigma(r)$ as a function of F_J derived in

§3.1.3.1.1-3.1.3.1.3 for different physical regimes. In the interest of brevity we do not perform this straightforward exercise here. For constant \dot{M} disks described by the solution (13) with $F_{J,0} = 0$ corresponding expressions for r^{sg} can be found in Goodman (2003) and Haiman et al. (2009). Other effects that may invalidate our treatment at large separations — low optical depth of the disk when Σ becomes small, neutrality of the disk at low T , etc. — have been previously discussed in Haiman et al. (2009).

4. DISK EVOLUTION.

Steady state solutions of the master equation (4) discussed so far require rather special circumstances to be realized globally, such as \dot{M} which is independent of r . In real circumbinary disks this condition is difficult to realize, simply because the mass supply rate of the disk at large separations \dot{M}_∞ is determined by processes that have nothing to do with the central binary. At the same time \dot{M} in the inner disk is set by the binary torque, and is in general different from \dot{M}_∞ .

Because of this mismatch of \dot{M} in different parts of the disk gas has to accumulate somewhere and this naturally leads to the evolution of disk properties. As we will see later evolution typically leads to the establishment of the quasi-steady state in the inner parts of the disk, where one can then apply the results obtained in previous section. To understand this process we need to obtain the time-dependent solutions of equation (4). This necessarily requires specifying the dependence of the diffusion coefficient D_J given by equation (5) upon l and F_J and a set of boundary conditions.

With a rare exceptions discussed in §4.2 we will always assume that the circumbinary disk starts out as a conventional constant \dot{M} disk in which

$$F_J(t = 0, l) = \dot{M}_\infty l, \quad (48)$$

see equations (14) and (17). This is a natural assumption for a viscously evolving disk, which is supplied by a source of mass located at $r \gg r_b$. Indeed, as the mass flows in, the viscous time in the disk decreases with r causing its structure to converge to that of a standard constant \dot{M} disk. When the inner edge of the disk approaches the semi-major axis of the binary, the latter starts tidally interacting with the disk providing a source of angular momentum. Tidal torque on the disk rapidly increases and stops the mass inflow at some radius r_{in} (or, equivalently, some value of the specific angular momentum l_{in}), which is comparable to the semi-major axis of the binary. We consider evolution of the disk starting from this moment and use an inner boundary condition in the form

$$\left. \frac{\partial F_J}{\partial l} \right|_{l=l_{in}} = \dot{M}(l_{in}) = \chi \dot{M}_\infty, \quad (49)$$

see equation (12).

In some cases one can solve equation (4) analytically, which is useful for qualitative understanding of the more complicated situations. In particular, for $D_J = \text{const}$ with initial and boundary conditions specified by equations (48) and (49) correspondingly one finds the following solution (with l playing role of spatial coordinate):

$$F_J(t, l) = \chi \dot{M}_\infty l + (1 - \chi) \dot{M}_\infty$$

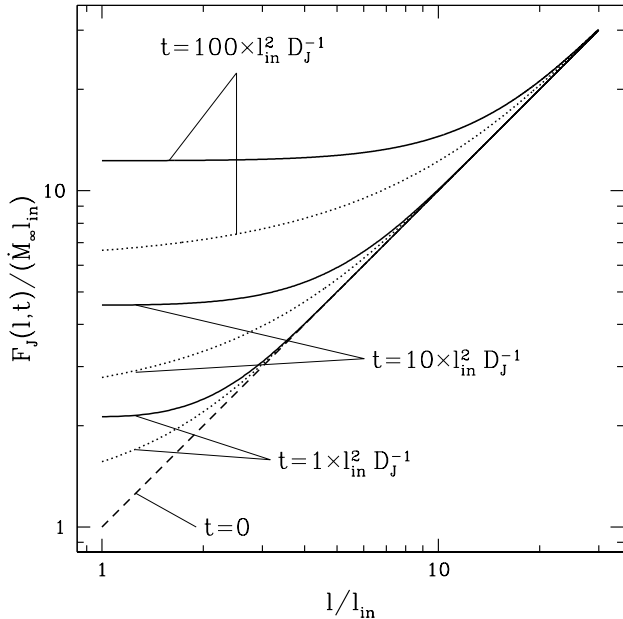


FIG. 2.— Time evolution of the angular momentum flux distribution $F_J(l, t)$ (l is the specific angular momentum acting as a space-like coordinate) in a disk with constant D_J (see Eq. [50]) and different boundary conditions imposed at the inner disk radius r_{in} , at which the specific angular momentum is l_{in} : $\dot{M}(l_{in}) = 0$ (solid lines) and $\dot{M}(l_{in}) = 0.5\dot{M}_\infty$ (dotted lines). The initial distribution of $F_J(l, 0) = \dot{M}_\infty l$ assumes a standard constant $\dot{M} = \dot{M}_\infty$ disk and is shown by a dashed line. Snapshots of F_J at different moments of time (labeled on the Figure) are shown.

$$\times \left\{ l_{in} + (l - l_{in}) \operatorname{erf} \left(\frac{l - l_{in}}{2\sqrt{D_J t}} \right) + \left(\frac{4D_J t}{\pi} \right)^{1/2} \exp \left[-\frac{(l - l_{in})^2}{4D_J t} \right] \right\}. \quad (50)$$

This solution is shown in Figure 2 for different values of $\dot{M}(l_{in})$ at different moments of time. One can clearly see that as the time goes by the influence of the central binary extends to larger and larger values of l , implying also larger distance from the central binary r . The transition from the initial distribution of F_J given by equation (48) to F_J strongly affected by the binary torque occurs at⁵ $l = l_{infl} \sim (D_J t)^{1/2}$.

Note that the solution for $\dot{M}(l_{in}) = 0$ ($\chi = 0$) clearly exhibits an inner region with $F_J \rightarrow \text{const}$, in agreement with our discussion of $\dot{M} = 0$ solutions in §2.2.2. At the same time the solution for $\dot{M}(l_{in}) = 0.5\dot{M}_\infty$ ($\chi = 0.5$) develops an inner region with F_J linearly increasing with l , again in complete agreement with the solution (13) with $F_{J,1} \neq 0$. Note that the torque exerted on the disk by the binary $F_J(l_{in})$ is quite different in two cases: it is smaller for larger values of χ which is natural since higher χ implies less mass accumulation at the inner edge of the disk and less torque exerted by the binary on the disk. This means that higher χ (higher $\dot{M}(l_{in})$) should result in slower inspiral of the binary.

⁵ Here we follow the notation of IPP, who called the radius at which this transition occurs the “radius of influence” r_{infl} .

We show next that the main features of disk evolution illustrated for the $D_J = \text{const}$ remain valid for the more general behavior of D_J . Following Filipov (1984), Lyubarskij & Shakura (1987), Pringle (1991), IPP, and Lipunova & Shakura (2000) we now derive self-similar solutions for evolving structure of an externally fed and centrally torqued circumbinary disk, allowing for the possibility of some mass overflow across the orbit of the secondary. Based on these solutions we then outline in §4.4.2 a general picture of the non-self-similar disk evolution.

4.1. Self-similar solutions for circumbinary disk evolution.

In §3 we demonstrated that in a variety of situations disk properties can be expressed as power laws of different physical parameters — F_J , r (or, equivalently, l), M_c , etc. Based on that we show in Appendices A & B that the diffusion coefficient in different regimes can be generically expressed in terms of the angular momentum flux F_J and specific angular momentum l in the power law form

$$D_J = D_{J,0} F_J^d l^p, \quad (51)$$

where d and p are constant power law indices. The explicit expressions for $D_{J,0}$, d , and p in relevant regimes can be found in Appendix B.

Equation (4) with D_J in the form (51) admits a self-similar solution⁶ provided that the problem at hand has no intrinsic scale. In circumbinary disks the inner edge of the disk (comparable to the semi-major axis of the binary) sets a natural scale. However, after the angular momentum injected by the binary has been transmitted by viscosity out to distances large compared to the radius of the inner cavity, this scale should not affect system’s behavior and evolution becomes self-similar.

To illustrate this point let us consider the solution (50) corresponding to a particular case of $d = p = 0$ in the limit of $t \gg l_{in}^2/D_J$, so that $l_{infl} \gg l_{in}$ (or $r_{infl} \gg r_{in}$). In this limit we can rewrite the solution (50) as

$$F_J(t, l) = \dot{M}_\infty \sqrt{D_J t} \left[\chi \xi + (1 - \chi) \xi \operatorname{erf} \left(\frac{\xi}{2} \right) + (1 - \chi) \frac{2}{\sqrt{\pi}} \exp \left(-\frac{\xi^2}{4} \right) \right]. \quad (52)$$

where $\xi = l/\sqrt{D_J t}$ is the dimensionless coordinate, which, as we will see later, plays the role of an independent self-similar variable. It is clear from this result that at late times the solution of the evolutionary equation (4) for $D_J = \text{const}$ is indeed independent of the exact value of l_{in} at which the inner boundary condition is imposed, and one can effectively set l_{in} to zero thus eliminating any intrinsic scales from the problem at hand.

In general case of arbitrary d and p in the expression (51) we first define new variables

$$f_J \equiv \frac{F_J}{M_\infty}, \quad \tau \equiv D_{J,0} \dot{M}_\infty^d t, \quad (53)$$

transforming equation (4) into

$$\frac{\partial}{\partial \tau} f_J^{1-d} = l^p \frac{\partial^2 f_J}{\partial l^2}, \quad (54)$$

⁶ Previously Lyubarskij & Shakura (1987) derived such solutions for F_J assuming boundary conditions different from what we use here.

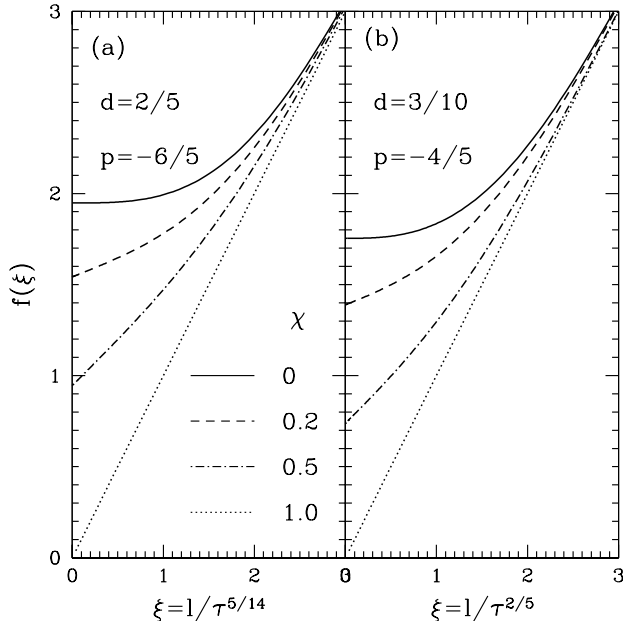


FIG. 3.— Behavior of the self-similar function f vs the variable ξ defined in equation (56). Different panels correspond to different values of the power law parameters d and p : (a) gas pressure dominated case with $\kappa = \kappa_{es}$, (b) gas pressure dominated case with $\kappa = \kappa_{ff}$. Various curves represent the run of $f(\xi)$ for different boundary conditions imposed at the inner edge, allowing for the possibility of mass inflow past the secondary orbit: $\dot{M}(0) = \chi \dot{M}_\infty$.

with the boundary condition

$$\left. \frac{\partial f_J}{\partial l} \right|_{l=0} = \frac{\dot{M}(l=0)}{\dot{M}_\infty} = \chi, \quad (55)$$

(instead of equation [49]), where $\chi \leq 1$ and may be equal to zero.

One can easily see that equation (54) admits self-similar solutions in the form

$$f_J = \tau^n f(\xi), \quad \xi \equiv \frac{l}{\tau^n}, \quad n = -\frac{1}{d+p-2}, \quad (56)$$

where function f satisfies ordinary differential equation

$$f'' f^d \xi^p = n(1-d)(f - \xi f') \quad (57)$$

with the boundary conditions

$$f'(\xi \rightarrow 0) = \chi, \quad f'(\xi \rightarrow \infty) = 1, \quad (58)$$

where the second boundary condition follows directly from the initial condition (48). Note that for $d = p = 0$ equation (56) reproduces the similarity seen in the analytical solution (52) obtained for constant D_J . We also verified the self-similar scalings of Σ derived in IPP for $\chi = 0$ case.

In Figure (3) we show the solutions of this equation for different values of mass accretion rate across the orbit of the secondary parametrized by the value of χ (generalizing results of IPP to the case of non-zero χ). We have chosen two sets of d and p corresponding to astrophysically relevant situations: gas pressure dominated regime with $\kappa = \kappa_{es}$ ($d = 2/5, p = -6/5, n = 5/14$), and with $\kappa = \kappa_{ff}$ ($d = 3/10, p = -4/5, n = 2/5$), see Appendix B

or Lyubarskij & Shakura (1987). We will see later in §5 that the radius of influence often extends into the parts of the disk where one of these regimes is valid.

As expected, the transition from the outer solution $f(\xi) = \xi$ unaffected by the binary torque to the inner solution influenced by it always occurs at $\xi \approx 1-2$. This transition clearly corresponds to the radius at which the viscous time in the disk t_{visc} is equal to the evolution time t of the system, i.e. the time that has passed since the central binary started tidally interacting with the disk at its inner edge. In other words, $t_{visc}(\xi \sim 1) \sim t$.

We take the radius of influence r_{infl} to correspond to $\xi_{infl} = 1$. Then, according to equations (53) and (56) the value of the specific angular momentum l_{infl} at r_{infl} is given by

$$l_{infl}(t) = \left(D_{J,0} \dot{M}_\infty^d \right)^n t^n, \quad r_{infl}(t) = \frac{l_{infl}^2(t)}{GM_c}, \quad (59)$$

while the viscous angular momentum flux in the disk is

$$F_J(l, t) = \dot{M}_\infty l_{infl}(t) \times f(l/l_{infl}(t)), \quad (60)$$

where the value of $f(\xi)$ can be found from Figure 3 for a given χ .

The torque acting on the central binary in the limit $l_{in} \ll l_{infl}(t)$ (or $r_{in} \ll r_{infl}(t)$) is given simply by $F_J(0, t) = \dot{M}_\infty l_{infl}(t) f(0, \chi)$ where the dependence of $f(0, \chi)$ upon the efficiency χ of mass inflow through the secondary orbit is shown in Figure 4 for different types of disks. One can see in complete analogy with the analytical solution (50) that allowing for some mass flow across the orbit of the secondary (i.e. assuming non-zero χ) leads to the reduction of the torque acting on the binary.

It might seem surprising that the torque experienced by the binary is independent of the mass of the secondary — $F_J(0, t)$ is set only by \dot{M}_∞ and $l_{infl}(t)$, since it is the potential of the secondary that gives rise to the tidal coupling with the disk. We comment on this point in §5.

4.2. General description of the disk evolution.

In §4.1 we outlined main features of the self-similar evolution of a circumbinary disk which arises when the three essential conditions are met: (1) the behavior of the diffusion coefficient D_J is given by a simple power law form (51), (2) the outer parts of the disk are well approximated by a standard constant \dot{M} disk with $F_J = \dot{M}_\infty l$, and (3) the radius of influence r_{infl} far exceeds the semi-major axis of the central binary r_b (and the radius of the inner disk edge r_{in}). We now describe how the picture of the disk evolution changes when these assumptions are relaxed by concentrating on the situation when there is no mass inflow across the orbit of the secondary, i.e. $\chi = 0$ or $\dot{M}(r_{in}) = 0$. More complicated setup allowing for some mass inflow across the orbit of the secondary can be understood by generalization of the picture that emerges in $\dot{M}(r_{in}) = 0$ case.

Different parts of circumbinary disks can feature different physical regimes as illustrated in §3. In this case a simple form of D_J given by equation (51) will not work in the whole disk invalidating global self-similarity. However, D_J can still be cast in this form in certain distance intervals with power law indices d and p intrinsic to each region. For example, one can easily imagine that the inner disk is in the radiation pressure dominated regime,

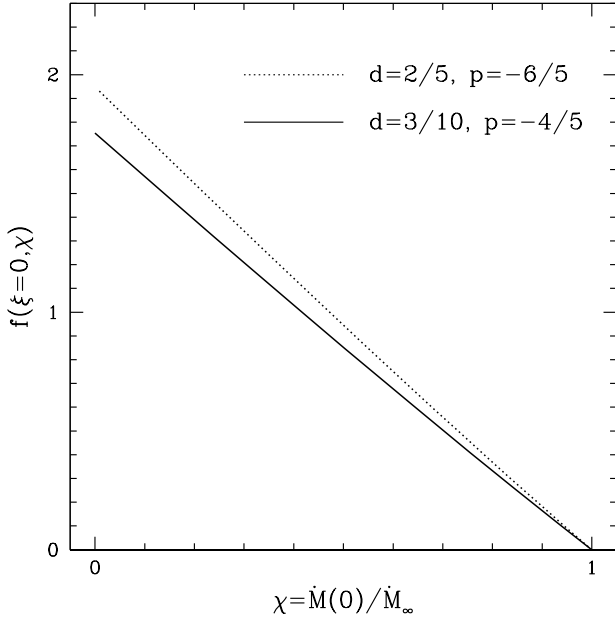


FIG. 4.— Value of $f(\xi = 0, \chi)$ as a function of χ — the fraction of \dot{M}_∞ passing through the orbit of the secondary. Different curves correspond to different values of the power law parameters d and p indicated on panels: (*dotted*) gas pressure dominated case with $\kappa = \kappa_{es}$, (*solid*) gas pressure dominated case with $\kappa = \kappa_{ff}$. Knowledge of $f(\xi = 0)$ allows computation of the torque acting on the central binary for arbitrary value of the “accretion fraction” χ .

while further out it transitions to gas pressure dominated regime with the opacity initially given by κ_{es} and then by κ_{ff} . In all these regimes one can locally use the power law description of D_J as described in Appendix B, with smooth transitions between the different scalings at the boundaries of different regimes.

Evolution equation written in the form (4) easily allows us to understand the behavior of the disk properties in this more complicated situation. Indeed, interior to r_{infl} the viscous time in the disk gets shorter with decreasing r , meaning that for $r \lesssim r_{\text{infl}}$ disk tends to approach a steady state solution. Then equation (4) implies that F_J in this part of the disk is given by a simple solution (13) *independent* of the complicated behavior of D_J caused by the transitions between different physical regimes. Disk properties such as $\Sigma(r)$, $T(r)$, etc. can be computed as functions of this radially constant F_J (for $\dot{M}(r_{in}) = 0$) using formulae derived in §3, and will show different dependence on r , F_J and other system parameters in different regimes.

At every moment of time the value of the radially constant (for $r \lesssim r_{\text{infl}}$) angular momentum flux F_J is obviously set by the the disk properties in a particular physical regime corresponding to $r \sim r_{\text{infl}}$. This regime can change in time since F_J steadily increases and both the transition radii of different regimes and r_{infl} vary. Nevertheless, it is clear that our results for the self-similar disk evolution obtained previously should allow one to easily understand even more complicated situations, see §5.

Second complication arises if the circumbinary disk does not start out as a standard constant \dot{M} disk with the initial distribution of the angular momentum flux in

the form (48) but is characterized by some more complicated initial distribution of $F_J(l, t = 0)$. Again, our understanding of the self-similar disks allows us to qualitatively characterize disk evolution in this case. The region influenced by the binary torque would still expand in time with the dependence $l_{\text{infl}}(t)$ given by an implicit relation

$$l_{\text{infl}}^2 \sim t \times D_J(F_J(l_{\text{infl}}, t = 0), l_{\text{infl}}), \quad (61)$$

see equation (4), in which we explicitly indicated the dependence of $D_J(F_J, l)$ on F_J and l . Interior to r_{infl} angular momentum flux is roughly constant with radius and equal to $F_J(l_{\text{infl}}(t), t = 0)$.

At the same time outside $r_{\text{infl}}(t)$ the disk will still maintain the distribution of F_J close to the initial distribution $F_J(l, t = 0)$ since the viscous time there is long compared to the system lifetime (which is also equal to $t_{\text{visc}}(r_{\text{infl}})$). If the initial distribution of F_J exhibits a maximum at some radius r_{max} then past the moment when $r_{\text{infl}} \sim r_{\text{max}}$ the circumbinary disk will turn into a decretion disk (Pringle 1991) and the mass accumulated in the central part of the disk will start flowing out, driven by continuing injection of the angular momentum by the binary (assuming that the binary does not merge by that time).

Finally, initially the radius of influence may not strongly exceed the radius of the inner edge of the disk. This is true if the evolutionary lifetime of the system has not yet exceeded the viscous time at the inner edge of the disk. However, at later times the condition $r_{\text{infl}} \gtrsim r_{in}$ is guaranteed to be fulfilled since r_{infl} steadily grows while both the binary semi-major axis and r_{in} can only decrease. As a result, at late times the system should inevitably converge to the self-similar mode of evolution (see e.g. evolution shown in Figure 2) or its generalizations described above for the more complicated situations.

5. IMPLICATIONS FOR SMBH BINARY EVOLUTION.

We now apply the results obtained in previous sections to the coupled evolution of SMBH binaries and disks around them. The two processes — orbital evolution of the binary and evolution of the disk properties — must be considered simultaneously because of their mutual influence on each other. In exploring this evolution one must pay special attention to the nonlocal effect of the binary torque on the disk.

Indeed, according to the results obtained in §4 the value of the angular momentum flux F_J carried through the disk near the binary (which determines the orbital evolution of the binary) is not set locally but is determined by the disk properties at the radius r_{infl} , which is the outermost radius affected by the viscous transport of the angular momentum deposited in the disk by the binary. This property, often omitted in previous studies of the SMBH binary evolution, is very important as we show further.

We emphasize that the torque acting on the binary, which according to equation (10) is equal to $F_J(r_{in})$, is independent of the mass of the secondary M_s and is the same irrespective of the mass ratio of the binary q (see also IPP). Also, the dependence of $F_J(r_{in})$ on the total mass of the binary M_c arises only because M_c determines the angular frequency in the disk. At first sight this may

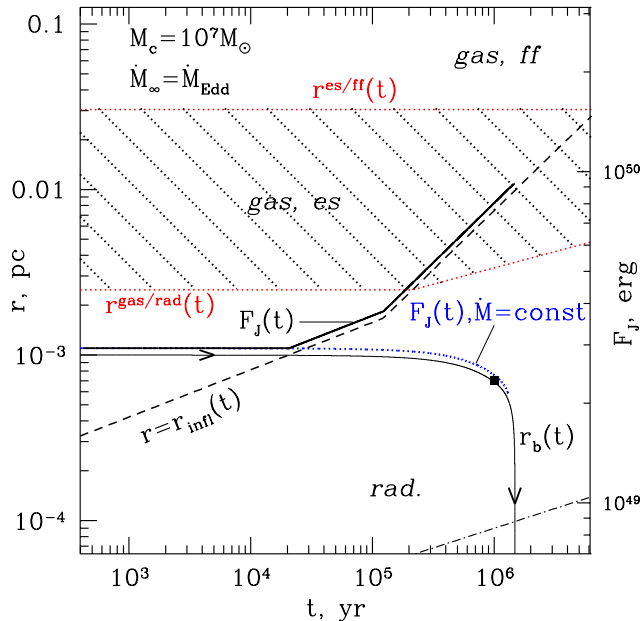


FIG. 5.— Characteristic evolution of the torque F_J (labeled on the right axis) experienced by the central binary with $M_c = 10^7 M_\odot$ and $q = 1$ as a function of time. Two cases are shown: $F_J(t)$ computed self-consistently accounting for the circumbinary disk evolution (thick black solid line) and assuming a standard constant \dot{M} disk from the binary is the same and equal to $\dot{M}_\infty = 10^{-2} \dot{M}_{\text{Edd}}$. Note the difference between the values of F_J computed in two ways for $t \gtrsim 10^5$ yr. Also shown is the orbital evolution of the binary (thin solid line) computed according to the first, self-consistent prescription for $F_J(t)$. Different regimes in which the disk can be present are labeled on the plot (red dotted lines $r^{\text{rad/gas}}$ and $r^{\text{es/ff}}$ show their boundaries) and the gas pressure-dominated case with $\kappa = \kappa_{\text{es}}$ is shaded. Dashed curve shows the run of $r^{\text{inf}}(t)$ in different regimes, and is closely related to the behavior of self-consistent $F_J(t)$. Eddington limit becomes important below the dot-dashed line in the lower right corner of the plot, see §5.2.5.2.5. Black square dot marks the transition from the disk- to GW-dominated orbital evolution of the binary. See text for more details.

seem strange since the strength of tidal interaction is determined by the potential of the secondary. However, one has to keep in mind that the full torque exerted by the binary on the disk is generally found to scale as (Goldreich & Tremaine 1980; Papaloizou & Lin 1984; Petrovich & Rafikov 2012)

$$F_J(r_{\text{in}}) \propto \frac{M_s^2 \Sigma_0}{\Delta^3}, \quad (62)$$

irrespective of the precise form of the torque density distribution. Here Σ_0 is the disk surface density just outside the region where the binary torques are important, and $\Delta = |r_{\text{in}} - r_b|$ is the width of the gap — the separation between the secondary orbit and the inner edge of the disk. Both $F_J(r_{\text{in}})$ and Σ_0 are set globally at the radius of influence.

Equation (62) shows that a particular value of the binary torque $F_J(r_{\text{in}})$ can be obtained not only by changing M_s but also by varying the width of the gap Δ for a given M_s , and this is how the disk-binary tidal interaction self-regulates itself to provide a necessary torque on the disk. As $F_J(r_{\text{in}})$ varies in time for a fixed M_s the

width of the gap should also vary. The same is true if one varies the mass of the secondary while keeping $F_J(r_{\text{in}})$ constant — the width of the gap would simply scale as $\Delta \propto q^{2/3}$. Of course, q cannot be arbitrarily small since a low mass secondary may not be able to prevent the mass flow across its orbit (e.g. if Δ needed to provide a given value of $F_J(r_{\text{in}})$ turns out being smaller than the disk scaleheight), meaning that the gap does not exist in the first place (see §5.2.5.2.6). But as long as the gap opening conditions are satisfied for a given q , the width of the gap should always be able to adjust itself to provide just the right amount of torque on the disk.

In our subsequent calculations we will not be directly addressing the “final pc” problem (Lodato et al. 2009) as we typically follow SMBH binaries starting at rather small separations, $10^{-2} - 10^{-4}$. Such binaries may be created by previous (possibly multiple) episodes of gas infall into the center of the galaxy in which the binary resides, each of which would tighten its orbit. At the same time some of our findings (e.g. significant reduction of the binary inspiral timescale when the disk evolution is self-consistently included) are likely to be relevant for attempting to resolve the “final pc” problem by accounting for the possibility of a circumbinary disk surrounding the binary.

In all our calculations we take the viscosity to scale with the total rather than the gas pressure in the radiation pressure dominated regime, i.e. $b = 0$. We will also assume that the tidal torque of the binary presents sufficiently strong barrier to inflowing gas to completely suppress gas overflow across the orbit of the secondary. This means that the boundary condition at the inner edge of the disk is given by $\chi = \dot{M}(r_{\text{in}})/\dot{M}_\infty = 0$. In principle one can easily extend our results on the orbital evolution of the binary to the case of $\chi \neq 0$. Finally, even though the binary itself is not accreting when $\dot{M}(r_{\text{in}}) = 0$ the inner parts of the disk are still gaining mass, which changes the potential in which gas orbits further out. In this work we are mainly concerned with the disk-related effects on the binary evolution and for that reason we neglect the increase of the binary+disk system mass throughout the calculation.

5.1. Binary inspiral: basic features.

We now look at the details of the orbital evolution of the binary SMBH embedded in a circumbinary disk. In Figure 5 we show the joint variation of the binary and the disk characteristics. The binary orbit is evolved according to

$$\frac{dr_b}{dt} = -\frac{r_b}{t_{\text{GW}}} - \frac{r_b}{t_J}, \quad (63)$$

where t_{GW} and t_J are given by equations (41) and (42). Variation of the disk properties, including the evolution of $F_J(r_{\text{in}})$ entering the equation (42), is described below.

We start an equal mass ($q = 1$) binary with the total mass $M_c = 10^7 M_\odot$ with initial semi-major axis of 10^{-3} pc. At time $t = 0$ disk properties correspond to a standard constant $\dot{M} = \dot{M}_{\text{Edd}}$ disk extending from very large distances (effectively from infinity) down to the binary semi-major axis (for simplicity we disregard the difference between the binary semi-major axis r_b and the inner radius of the disk, which is a factor of 2 uncertainly at most, see MacFadyen & Milosavljević 2008).

This setup would naturally arise if the binary initially resided in a gas-free environment and then gas started flowing into the galactic center in a disk-like configuration from large distances. Because viscous evolution accelerates at small radii the disk would naturally settle into a constant \dot{M} configuration. At some point its inner radius would reach the vicinity of the binary and tidal torque would stop the gas inflow. This moment represents the starting point for our calculations.

The radial dependence of disk properties at time $t = 0$ can be found in Haiman et al. (2009) or by setting $F_J = \dot{M}_\infty (GM_{cr})^{1/2}$ as appropriate for a standard constant \dot{M} disk in formulae derived in §3.1. As Figure 5 demonstrates the binary starts in the radiation pressure dominated part of the disk but the transition to the gas pressure dominated regime occurs not too far outside of r_b , at $r^{\text{rad/gas}} \approx 2.5 \times 10^{-3}$ pc. Opacity switches from being dominated by the electron scattering to free-free opacity at $r^{\text{es/ff}} \approx 0.03$ pc. These regimes are clearly labeled in Figure 5.

We also show the run of the radius of influence $r_{\text{infl}}(t)$ in time by a dashed curve. At $r = r_{\text{infl}}(t)$ the local viscous time equals the time since the start of the evolution t but this is meaningful only if at time t the disk extends to $r < r_{\text{infl}}(t)$, which is not always the case. Nevertheless, this dependence is still a useful concept as it allows us to see important transitions in the disk properties if we were to take an initial SMBH semi-major axis $r_b(0)$ different from the value shown in Figure 5. The actual dependence $r_{\text{infl}}(t)$ is calculated using definition (59) and the expressions for $D_{J,0}$, d and n that can be found in Appendix B. Since these expressions are different in various physical regimes the behavior of $r_{\text{infl}}(t)$ exhibits distinct transitions as it crosses the boundaries of different regimes, clearly visible in Figure 5.

As the binary starts tidally interacting with the disk the inflowing material begins accumulating near the inner edge of the disk. In addition to the evolution of the binary orbit (thin solid curve) this Figure also shows the time behavior of the torque $F_J(r_{in}, t)$ at the inner edge of the disk (thick solid curve calibrated on the right axis), which is absorbed by the binary and causes its orbital evolution. The $F_J(r_{in}, t)$ curve initially closely follows⁷ $r_b(t)$ because the torque exerted on the binary by a constant \dot{M} disk is well approximated by $F_J(r_{in}, t) = \dot{M}_\infty (GM_c r_b)^{1/2}$ as long as the inner edge of the disk tracks the binary orbit. This torque is small enough for r_b not to change appreciably for rather long time.

Approximately at $t = 2 \times 10^4$ yr, when $t_{\text{visc}}(r_b(0)) \sim t$, the radius of influence of the binary torque r_{infl} grows beyond the initial binary semi-major axis $r_b(0)$. As a result, angular momentum flux at the inner edge of the disk $F_J(r_{in}, t)$ starts increasing as $F_J(r_{in}, t) \propto l_{\text{infl}}(t) \propto t^{1/7}$ thus accelerating the orbital evolution of the binary. Unlike the calculations of the self-similar disk behavior in §4.1 in our present calculation we do not consider the details of the smooth transition between the parts of the disk inside and outside of r_{infl} . Instead we simply assume that $F_J(r, t) = \dot{M}_\infty l$ for $l > l_{\text{infl}}(t)$ as appropriate for a

constant \dot{M} disk, while $F_J(r, t) = \dot{M}_\infty l_{\text{infl}}(t)$ is constant in space for $l < l_{\text{infl}}(t)$. In other words, we adopt a simple piece-wise dependence of F_J on r :

$$F_J(r, t) = \begin{cases} \dot{M}_\infty (GM_{cr})^{1/2}, & r > r_{\text{infl}}(t), \\ \dot{M}_\infty [GM_c r_{\text{infl}}(t)]^{1/2}, & r \leq r_{\text{infl}}(t), \end{cases} \quad (64)$$

For that reason at late times $F_J(r_{in}, t)$ starts tracking the run of $r_{\text{infl}}(t)$ in Figure 5.

Initially r_{infl} stays in the radiation pressure dominated regime and varies as $r_{\text{infl}} \propto t^{2/7}$, see equations (59) and (B1). At $t \approx 2 \times 10^5$ yr the radius of influence reaches out into the gas pressure dominated regime with $\kappa = \kappa_{es}$. There r_{infl} grows as $r_{\text{infl}} \propto t^{5/7}$ (see the break in slope of r_{infl} curve), and the increase of $F_J(r_{in}, t)$ and of the torque acting on the binary accelerates.

In our calculations the disk interior to $r = r_{\text{infl}}$ is a constant F_J disk (see equation [64]) with properties explored in §3.1 rather than a constant \dot{M} disk present outside of the radius of influence. As the value of F_J in the inner disk grows the disk properties keep changing as well. In particular the boundaries of the different regimes, i.e. $r^{\text{rad/gas}}$ and $r^{\text{es/ff}}$, expand as the time goes by. Thus, the state of the disk at the location of the binary may change not only because of the variation of the binary orbit, but also due to the disk evolution, see Figures 6 & 7.

Note, that even though in the calculation shown in Figure 5 the binary is always in contact with the radiation pressure dominated region of the disk, beyond $t \approx 2 \times 10^5$ yr the torque on the binary is determined by the gas pressure dominated part of the disk with $\kappa = \kappa_{es}$, since this is where r_{infl} is. This demonstrates the nonlocality of the disk influence on the binary — the state of the disk near the binary is essentially irrelevant for its orbital evolution. It is what goes on in the disk at $r \sim r_{\text{infl}}$ that determines the torque acting on the SMBH binary at late times.

This fact has been overlooked in previous studies of the gas-assisted SMBH inspiral problem. In particular, Haiman et al. (2009) and Kocsis et al. (2011) used the self-similar results of SC95 and IPP to account for the mass accumulation in the disk near the binary orbit. However, in their calculations they have effectively assumed that the radius of influence r_{infl} corresponds to the same regime of the disk in which the binary is currently residing. In the case shown in Figure 5 this would mean that even after 2×10^5 yr the increase of r_{infl} with time would be calculated according to the scaling for the radiation pressure dominated regime, leading to an *underestimate* of the torque acting on the binary and an *overestimate* of its inspiral time. Our calculations fully take into account the nonlocality of the disk influence on the disk.

To better illustrate the role of mass pileup and disk evolution for the orbital evolution of the binary we compare our results with calculations in which disk properties remain well represented by the properties of a constant \dot{M} disk at all times. Then the torque on the binary is always given by $F_J(t) = \dot{M}_\infty [GM_c r_b(t)]^{1/2}$, see dotted curve in Figure 5. Clearly, this torque can be much smaller than the real $F_J(t)$, especially at late times, meaning that such calculations should overestimate the inspiral time of the binary.

⁷ For clarity we have slightly shifted the curve $F_J(r_{in}, t)$ upward in Figure 5 to avoid overlap with other curves, e.g. $r_b(t)$.

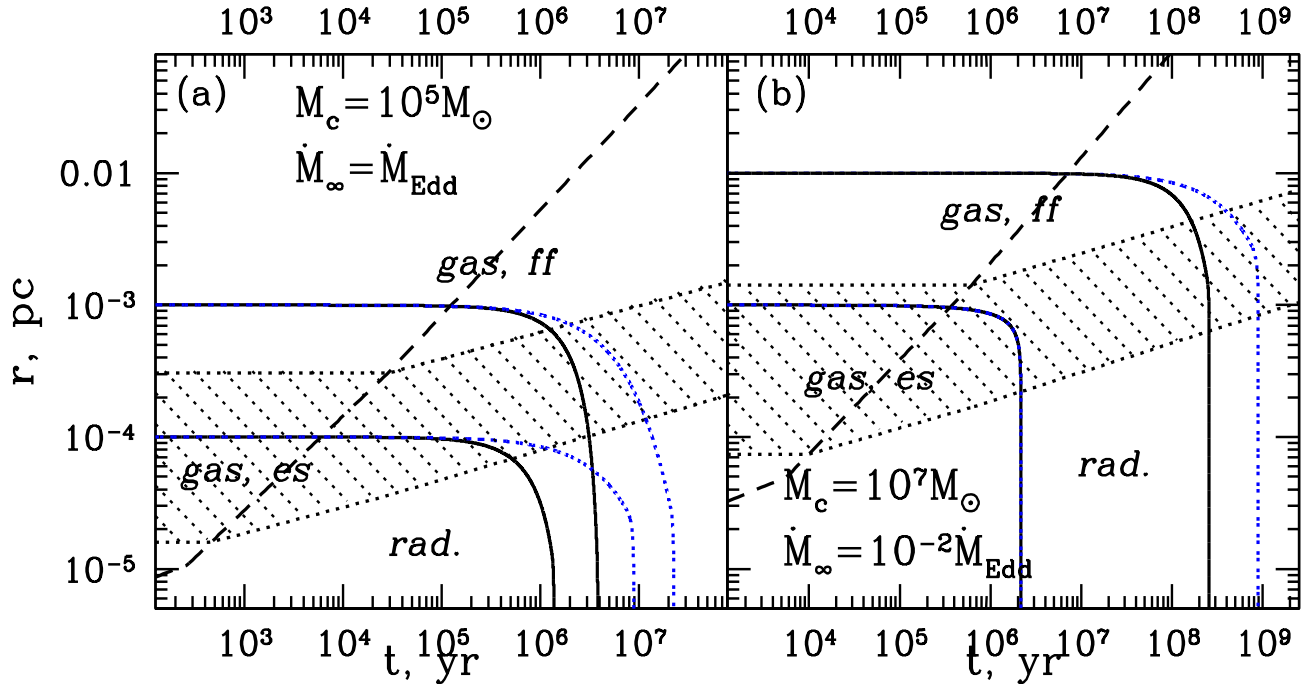


FIG. 6.— Comparison of the orbital evolution of the SMBH binary computed in two ways: fully accounting for the disk evolution driven by the tidal torque of the binary (*solid black curves*) and simply assuming the disk properties to be given by a standard constant \dot{M} solution (*dotted blue curves*). In both cases the value of \dot{M}_∞ , initial semi-major axis of the binary, and all other parameters are assumed to be the same. Results are shown for $M_c = 10^5 M_\odot$, $\dot{M}_\infty = \dot{M}_{\text{Edd}}$ (panel a) and for $M_c = 10^7 M_\odot$, $\dot{M}_\infty = 10^{-2} \dot{M}_{\text{Edd}}$ (panel b), with binary mass ratio $q = 1$ in all cases. Meaning of other curves and labels on these plots is the same as in Figure 5. Note that properly accounting for the binary-driven disk evolution can reduce the lifetime of the binary by almost an order of magnitude in some cases.

In Figure 6 we display $r_b(t)$ calculated using constant \dot{M} disk properties (dotted curves) and fully accounting for the binary-driven disk evolution (solid curves) for two equal mass ($q = 1$) SMBH binary+disk systems: one with $M_c = 10^5 M_\odot$, $\dot{M}_\infty = \dot{M}_{\text{Edd}}$ and another with $M_c = 10^7 M_\odot$, $\dot{M}_\infty = 10^{-2} \dot{M}_{\text{Edd}}$. Two different starting radii $r_b(0)$ are explored in both cases.

One clearly sees that in most cases evolution of r_b computed using standard constant \dot{M} disk properties considerably overestimates (by almost an order of magnitude in some cases) the binary inspiral time. In the case of $M_c = 10^7 M_\odot$, $\dot{M}_\infty = 10^{-2} \dot{M}_{\text{Edd}}$, and $r_b(0) = 10^{-3}$ pc the evolutionary tracks of the binary computed by two methods coincide. This is because in this case GW emission is more important for the evolution of the binary than the tidal coupling to the disk at all times, resulting in a universal behavior of $r_b(t)$. But whenever disk torques are important, binaries shrink faster when the self-consistent disk evolution is properly taken into account. For that reason, we strongly discourage the use of standard constant \dot{M} disk properties for exploring the evolution of the central binary of a circumbinary disk.

5.2. Binary inspiral: parameter exploration.

In Figures 7 & 8 we provide a more detailed and systematic view of the SMBH binary evolution under different conditions. We explore two representative values of M_c : $10^5 M_\odot$ (implying Schwarzschild radius $R_S = 10^{-8}$ pc) and $10^7 M_\odot$ ($R_S = 10^{-6}$ pc), but our results can be trivially extended to other values of M_c . Accretion rate in the disk at large distances is taken to be either

$\dot{M}_\infty = 10^{-2} \dot{M}_{\text{Edd}}$ or \dot{M}_{Edd} , and binary mass ratio is varied between $q = 10^{-2}$ and 1. We also consider two different values of the starting semi-major axis of the binary $r_b(0)$: 10^{-4} pc and 10^{-3} pc for $M_c = 10^5 M_\odot$, and 10^{-3} pc and 10^{-2} pc for $M_c = 10^7 M_\odot$. These values are close to the “bottleneck” semi-major axes at which the stellar dynamical orbital evolution of SMBH pairs decelerates dramatically, see Yu (2002).

One might worry that the outer parts of the disk can be prone to gravitational instability. We determined that in the initial constant \dot{M} disk Toomre Q equals unity at $r^{sg} = 9 \times 10^{-3}$ pc, 0.3 pc, 0.3 pc, and 0.5 pc for the systems shown in panels (a)-(d) correspondingly in Figure 7 (for $\alpha = 0.1$, $\varepsilon = 0.1$, $\mu = 0.5m_p$). Thus, at the start of our calculations one needs to worry about the importance of the disk self-gravity only for the system with $M_c = 10^7 M_\odot$, $\dot{M}_\infty = \dot{M}_{\text{Edd}}$ and the binary starting at $r_b(0) = 10^{-2}$ pc, where the disk can be marginally gravitationally unstable. One has to keep in mind though that later the torque on the binary is going to be set at the radius of influence that expands beyond $r_b(0)$, see §5.1. If r_{infl} would exceed r^{sg} at some point, the calculations of disk evolution would need to be refined. In our present study we neglect this complication; it may only be an issue for the high-mass systems shown in Figure 7a.

Figure 7 shows evolutionary tracks of the binary orbit mapped onto the disk state in the format analogous to that used in Figures 5 & 6. In addition, in Figure 8a,b we show the dependence of the binary orbital evolution timescale $t_{\text{ev}} \equiv -r_b/\dot{r}_b$ vs. the binary orbital period P_{orb} or semi-major axis r_b (upper axis) for the evolutionary

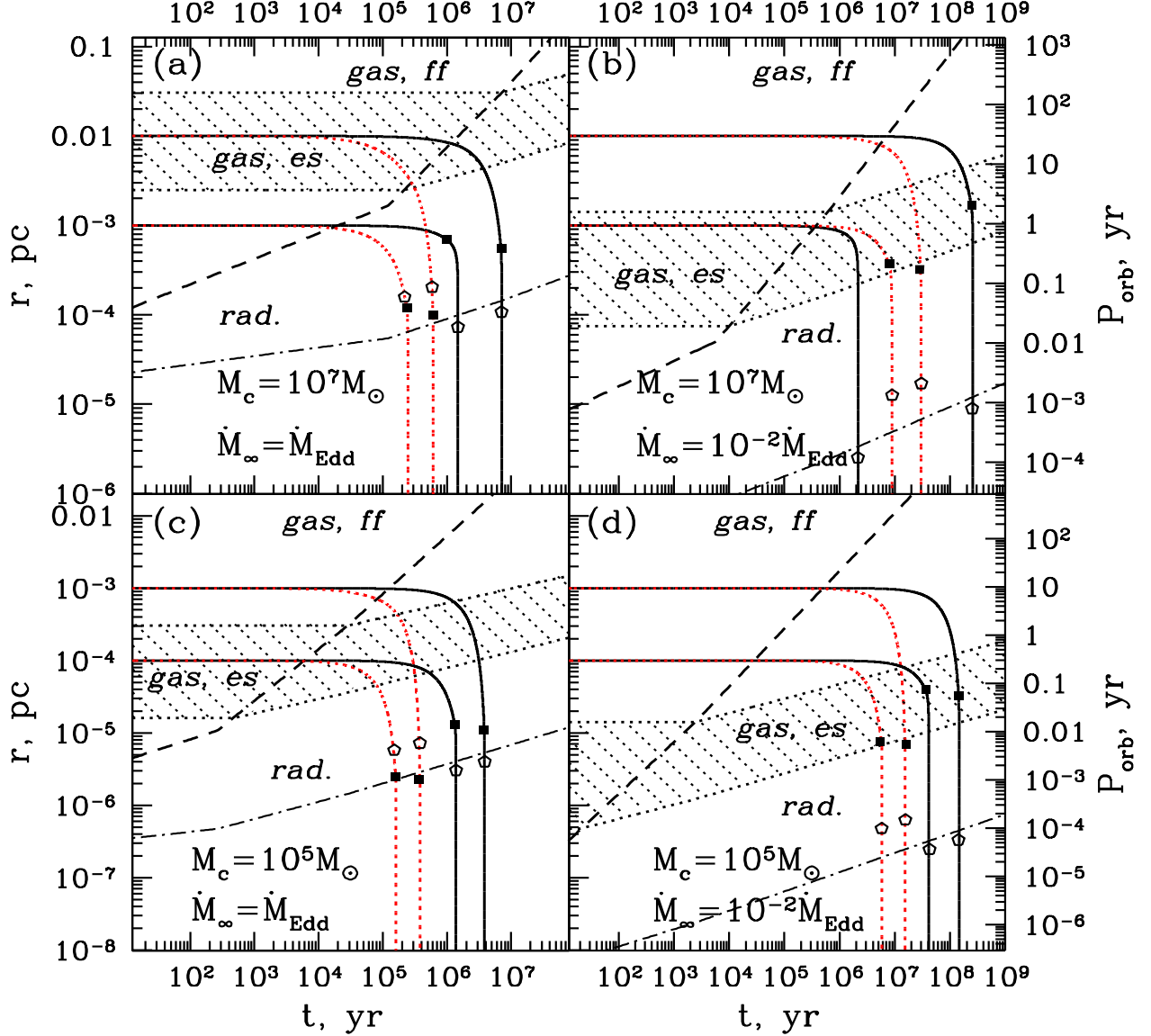


FIG. 7.— Evolutionary tracks of SMBH binaries for different values of $M_c = 10^7, 10^5 M_\odot$ and $\dot{M}_\infty/\dot{M}_{\text{Edd}} = 1, 10^{-2}$, labeled on panels. Tracks for $q = 1$ (solid black) and 10^{-2} (dotted red) are shown and in each panel we consider two starting values of the binary semi-major axis $r_b(0)$. Layout of these plots and meaning of different curves and labels are the same as in Figure 5. In particular, dashed and dot-dashed curves show the run of r_{inf} (equation [59]) and r_{Edd} (equation [65]) correspondingly, and black square dots mark the transition to the GW-dominated orbital decay. Open pentagons mark the possible onset of the gas overflow, see §5.2.5.2.6. See text for detailed description of evolution.

tracks displayed in Figure 7. This plot allows us to easily see the transition from the disk dominated evolution at longer periods to the GW dominated phase, which is clearly described by straight line tracks at small values of P_{orb} . Figure 8a,b can be directly compared to the analogous $t_{\text{ev}}(P_{\text{orb}})$ plots in Haiman et al. (2009).

Results presented in Figures 7 & 8 can be summarized in the following set of conclusions.

5.2.1. Circumbinary disk can be efficient in driving orbital evolution of the binary.

We generally agree with the results of existing studies (e.g. IPP, Haiman et al. 2009) that disks can appreciably accelerate orbital evolution of SMBH binaries. Figures

7 & 8 clearly illustrate this point. According to equation (41) without the disk the orbital evolution timescale due to emission of gravitational waves is rather long for some of the systems shown in these plots: for example, $t_{\text{GW}} = 8.3 \times 10^{10}$ yr for equal mass $10^7 M_\odot$ SMBH binary starting at $r_b(0) = 10^{-2}$ pc. Systems with small mass ratios evolve even slower: a binary with $q = 10^{-2}$ takes ≈ 25 times longer to merge due to the GW emission alone. The only system in our sample strongly affected by the GW emission from the very start is the equal mass $10^7 M_\odot$ binary starting at 10^{-3} pc and surrounded by a disk with $\dot{M}_\infty = 10^{-2} \dot{M}_{\text{Edd}}$, see Figure 8a. As expected this system merges faster than its $q = 10^{-2}$ counter-

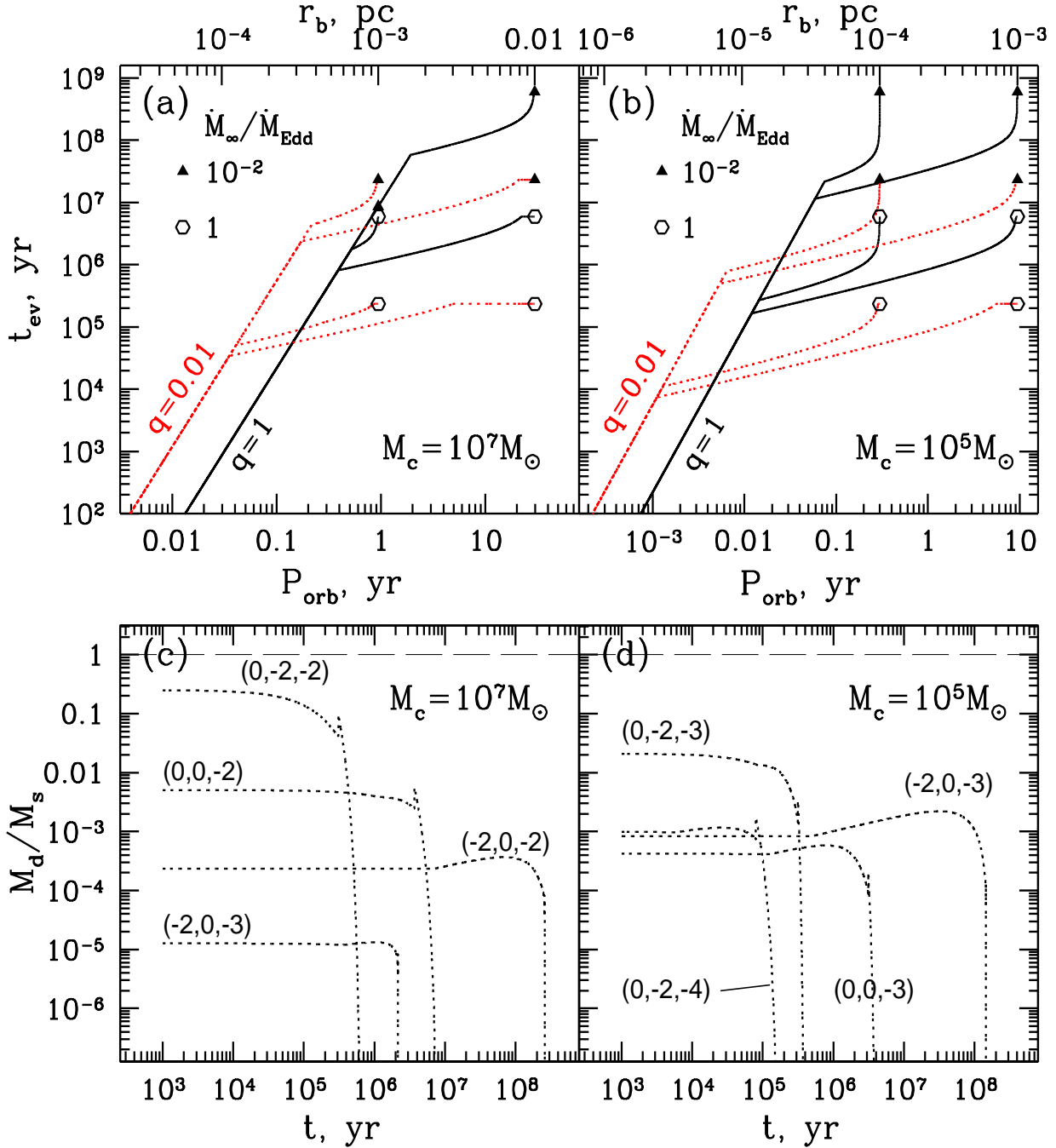


FIG. 8.— (a,b) Evolution timescale $t_{ev} = |d \ln r_b/dt|^{-1}$ of SMBH binaries as a function of orbital period P_{orb} or semi-major axis r_b (upper axis; use to read off the initial semi-major axis $r_b(0)$). Starting points for each evolutionary track are marked by either triangles (for $\dot{M}_\infty = 10^{-2}\dot{M}_{Edd}$) or hexagons (for $\dot{M}_\infty = \dot{M}_{Edd}$). Solid (black) and dotted (red) curves are used for $q = 1$ and $q = 10^{-2}$ binary tracks. Straight portions of these tracks at low P_{orb} correspond to the epoch when the orbital evolution of the binary is dominated by the GW emission. Note that prior to that tracks starting at different $r_b(0)$ do not overlap, illustrating hysteresis of the binary evolution caused by the non-local nature of the self-consistent disk-binary coupling. (c,d) Ratio of the local disk mass M_d to the secondary mass M_s for a sub-sample of evolutionary tracks displayed in Figure 7, showing that $M_d/M_s \ll 1$ in our calculations. Different tracks are labeled as $(\log[\dot{M}_\infty/\dot{M}_{Edd}], \log q, \log[r_b(0)/\text{pc}])$. See text for details.

part, even though the latter is affected more by the disk torques.

On the other hand, the same $q = 1$, $10^7 M_\odot$ binary starting at $r_b(0) = 10^{-2}$ pc and surrounded a disk accreting at $\dot{M}_\infty = \dot{M}_{Edd}$ merges within 7 Myr — more than 4 orders of magnitude faster than without the disk!

Lower mass disks are of course less efficient at driving orbital evolution of SMBH binaries — the same binary surrounded by a disk with $\dot{M}_\infty = 10^{-2}\dot{M}_{Edd}$ merges within 3×10^8 yr, but this is still much shorter than the corresponding t_{GW} . Lower mass ratio binaries are affected by the disk even stronger, provided that they present an

efficient barrier to the mass inflow at the orbit of the secondary. For example, $10^7 M_\odot$ binary with $q = 10^{-2}$ surrounded by a disk with $\dot{M}_\infty = 10^{-2} \dot{M}_{\text{Edd}}$, merges within 3×10^7 yr, about an order of magnitude faster than the $q = 1$ binary with the same parameters.

In Figure 7 black square dots mark the location on the evolutionary track of each SMBH binary where the disk dominated evolution switches to the GW dominated orbital decay. In systems with massive, high- \dot{M}_∞ disks this transition typically occurs when the binary is in contact with the radiation pressure dominated part of the disk. However, in systems with less massive, lower- \dot{M}_∞ disks this transition may happen even while the binary is surrounded by the gas pressure dominated (with $\kappa = \kappa_{es}$) part of the disk.

Another way to state the importance of the disk dominated evolution is to note that in most cases transition to GW dominated regime occurs at $r_b \ll r_b(0)$, i.e. after the binary semi-major axis has been significantly reduced by the disk torques. For example, evolution of a $M_c = 10^5 M_\odot$ binary with $q = 10^{-2}$ starting at 10^{-3} pc is dominated by torques produced by a $\dot{M}_\infty = \dot{M}_{\text{Edd}}$ disk down to $r_b \approx 2 \times 10^{-6}$ pc, see Figure 7c. This is almost three orders of magnitude smaller than $r_b(0)$ and is about $200 R_S$ for the binary. This additionally emphasizes the important role of disk torques in shrinking the SMBH binary orbits, even at relatively large separations.

5.2.2. Nonlocal character of the disk-binary coupling

As described in §5.1 the torque exerted on the binary is set by the disk properties at r_{inff} . Initially binary can affect only its immediate surroundings as it takes certain time for the disk to absorb enough angular momentum injected by the binary to affect the surface density distribution further out in the disk. For that reason initially $F_J(r_{in})$ is essentially the same as in the case of a constant $\dot{M} = \dot{M}_\infty$ disk, and is set by the disk *locally*, at $r \sim r_b$. This torque is usually rather small implying slow orbital evolution and long values of t_{ev} .

However, after system has evolved for time comparable to the viscous timescale at the inner disk edge $t_{\text{visc}}(r_{in})$, r_{inff} starts exceeding r_b . Past that point the torque on the binary $F_J(r_{in})$ is being set *globally*, at distances far exceeding r_b , which can be clearly seen in several evolutionary tracks shown in Figure 7. Increase of $F_J(r_{in})$ initially occurs at almost constant r_b , which is reflected in almost vertical initial evolutionary tracks in $t_{ev} - P_{orb}$ plane shown in Figure 8a,b, clearly visible for $M_c = 10^5 M_\odot$ and low $\dot{M}_\infty/\dot{M}_{\text{Edd}} = 10^{-2}$.

Global nature of the torques is generally more pronounced for lower mass binaries and for lower \dot{M}_∞ . This is because higher M_c implies earlier transition to the GW-dominated orbital decay (see Figure 8a,b), shortening the binary lifetime and not allowing r_{inff} to extend as far as in the lower M_c case. Higher $\dot{M}_\infty/\dot{M}_{\text{Edd}}$ plays similar role, shortening the binary lifetime and reducing the radius of influence at the end of inspiral compared to the lower \dot{M}_∞ case. This is true even though r_{inff} itself depends on both M_c and \dot{M}_∞ — these dependencies are usually rather weak, see Appendix B.

Almost all tracks shown in Figure 7 at some point in their evolution run into the situation described in §5.1,

where the inner edge of the disk (assumed equal to r_b) and r_{inff} reside in parts of the disk corresponding to different physical regimes. This means that calculations of the binary evolution assuming the scaling of $r_{\text{inff}}(t)$ to always correspond to the physical state of the disk near the binary orbit (Haiman et al. 2009; Kocsis et al. 2011) are not accurate. Figure 7 demonstrates that using this simple-minded procedure for a binary in the radiation pressure-dominated regime can easily underestimate the torque $F_J(r_{in})$ driving its orbital evolution thus overestimating the binary lifetime (see e.g. Figure 7a,c). Analogously, for a binary residing in the gas pressure dominated regime with $\kappa = \kappa_{es}$ and r_{inff} extending into the part of the disk where $\kappa = \kappa_{ff}$ (see Figure 7b-d) the use of $r_{\text{inff}}(t)$ scaling corresponding to the binary location would again lead to a (mild) underestimate of $F_J(r_{in})$ ($r_{\text{inff}}(t) \propto t^{4/5}$ when $\kappa = \kappa_{ff}$) and an overestimate of the merger time.

Another consequence of the non-locality of the disk-binary coupling is the clear *hysteresis* in the evolution of the system — the dependence of the current rate of orbital decay of the binary on the previous history of the disk evolution. This property is most readily seen in Figure 8, in which the evolutionary tracks computed for the same M_c , q , \dot{M}_∞ but starting at different initial radii do not result in the same orbital decay timescale t_{ev} at a given orbital period in the disk-dominated regime. One can see that for a fixed P_{orb} the inspiral timescales computed for different starting conditions can differ by a factor of several. This is in contrast to local calculations presented in Haiman et al. (2009), in which orbital evolution depends only on the current value of r_b , see their Figures 1-5 showing just a single evolutionary track for a given set of M_c and q .

5.2.3. Evolution of the disk accelerates orbital evolution of the binary

Because the radius r_{inff} setting the value of the inner torque $F_J(r_{in})$ in our calculations (see equation [64]) steadily grows, we necessarily find the disk evolution to result in the *speed up* of the binary decay compared to the case in which the disk is a constant $\dot{M} = \dot{M}_\infty$ disk at all times. As we have shown in §5.1 this results in shorter lifetime of the system in our calculations, which is a very natural result.

Interestingly, previously Haiman et al. (2009) have reached a directly opposite conclusion — that the disk evolution caused by the mass pile up near the orbit of the secondary *slows down* its inspiral (see their Figures 6 & 7). Whether this difference is caused by the local character of the of the disk-binary coupling assumed by Haiman et al. (2009) or by the adoption of SC95 solution in their calculations is not clear.

5.2.4. Validity of the secondary dominated regime

In Figure 8c,d we display the ratio of the secondary mass M_s to the local disk mass $M_d = \Sigma(r_b)r_b^2$. Our calculations explicitly assume a “secondary-dominated” limit $M_d/M_s \lesssim 1$ (SC95; IPP; Haiman et al. 2009) since only in this case the boundary condition in the form (10) is valid, as discussed in §2.2.1. One can easily see that almost all evolutionary tracks shown in Figure 8c,d (which are also present in Figure 7) satisfy $M_d/M_s \ll 1$

and thus correspond to the secondary-dominated regime. This finding is in agreement with Haiman et al. (2009) conclusion on the ubiquity and importance of this stage of the binary evolution.

Evolutionary track for a $q = 10^{-2}$, $M_c = 10^7 M_\odot$ SMBH binary starting at 10^{-2} pc and surrounded by a disk accreting at $\dot{M}_\infty = \dot{M}_{\text{Edd}}$ shows the highest $M_d/M_s \sim 0.2$ at early stages of the evolution among all the tracks computed in this work. For this binary the secondary-dominated regime is close to being marginally violated, and its track exhibits noticeable evolution even prior to crossing $r_{\text{infl}}(t)$ curve. Whenever $M_d \sim M_s$ the inner part of the disk contains the amount of angular momentum comparable to the full orbital angular momentum of the binary at the very start of evolution. Thus, to cause appreciable evolution of the disk via tidal coupling (which happens on the local viscous timescale) and to push the radius of influence beyond $r_b(0)$ requires the binary to give off a noticeable fraction of its orbital angular momentum. As a result a massive disk is able to shrink the binary orbit very efficiently, in less than the local viscous timescale at the inner edge of the disk.

At even higher values of M_d/M_s one needs to employ a boundary condition (7) different from (10) to properly compute the disk evolution.

5.2.5. Importance of the Eddington limit

As we discussed in §3.13.1.4 the magnitude of the angular momentum flux in a constant F_J disk cannot be arbitrarily high, because of the existence of the Eddington limit (40) in the radiation pressure dominated region of the disk. We now check how important is this constraint for the SMBH binary evolution.

In Figure 7 we plot as a dot-dashed curve the Eddington radius r_{Edd} at which the Eddington limit becomes important. This dependence can be easily derived from equation (40) and reads

$$\begin{aligned} r_{\text{Edd}}(t) &= \left[\frac{\kappa_{es} F_J(t)}{2\pi c (GM_c)^{1/2}} \right]^{2/3} \\ &= \left(\frac{\kappa_{es} \dot{M}_\infty}{2\pi c} \right)^{2/3} r_{\text{infl}}^{1/3}(t), \end{aligned} \quad (65)$$

where the value of F_J in the inner part of the disk affected by the binary torque is assumed to be given by equation (64). In this expression we use the dependence $r_{\text{infl}}(t)$, which is also plotted in the same Figure. Eddington limit is important for a circumbinary disk whenever $r_b < r_{\text{Edd}}(t)$.

Figure 7 demonstrates that for our choices of M_c , q , \dot{M}_∞ and $r_b(0)$ the Eddington limit is essentially irrelevant during the disk-dominated phase of the orbital evolution of the binary: dot-dashed curve of $r_{\text{Edd}}(t)$ always passes below or close to the square dots marking the transition to the GW-dominated regime. This provides justification for our calculations of the binary evolution since the details of the disk physics, including the advent of the Eddington limit, are not going to affect it in the GW-dominated regime.

On the other hand, for all evolutionary tracks depicted in Figure 7 the Eddington limit does become important at some point and affects the disk properties right before

the binary merger. This may have important implications for the electromagnetic precursor of the merger.

It is worth stressing that the Eddington limit in a constant F_J disk can be easily reached even if the mass accretion rate in the disk at large separations is far less than \dot{M}_{Edd} , see Figure 7b,d. This is obviously caused by accumulation of mass at the inner edge of the disk resulting in higher temperature and more important role of the radiation pressure than in a constant \dot{M} disk. Thus, the Eddington limit in self-consistently evolved circumbinary disks is more stringent than in the standard constant \dot{M} disks.

At the same time, the Eddington limit is still less important for low values of $\dot{M}_\infty/\dot{M}_{\text{Edd}}$: for $\dot{M}_\infty = 10^{-2}\dot{M}_{\text{Edd}}$ it kicks in only at the distances of several tens of Schwarzschild radii at most, see 7b,d. At the same time for $\dot{M}_\infty = \dot{M}_{\text{Edd}}$ the Eddington limit starts affecting the disk near the binary as soon as the latter enters the GW-dominated regime.

5.2.6. Gas overflow across the orbit of the secondary

Our assumption⁸ of $\dot{M}(r_{\text{in}}) = 0$ adopted throughout most of this work is equivalent to demanding the width of the gap between the orbit of the secondary and the inner edge of the disk Δ to be larger than the disk scale-height h . Indeed, the torque density produced by the planet drops for $|r - r_b| \lesssim h$ due to the phenomenon of the ‘‘torque cutoff’’ (Goldreich & Tremaine 1980), which implies that the secondary can effectively repel the disk fluid only if the gap width satisfies $\Delta \gtrsim h$. When this condition is not fulfilled, gas enters the torque cutoff zone near the orbit of the secondary where the tidal repulsion is no longer effective and starts to overflow the orbit of the secondary (Kocsis et al. 2012). As a result, the inner boundary condition in the form $\dot{M}(r_{\text{in}}) \ll \dot{M}_\infty$ may get violated.

Following SC95 we can estimate the gap width as

$$\frac{\Delta}{h} \sim \left[\frac{q^2}{\alpha\beta^b} \left(\frac{r}{h} \right)^5 \right]^{1/3}, \quad (66)$$

where we assumed viscosity to be given by equation (23). In both the gas pressure and the radiation pressure dominated regime with $b = 0$ (which we adopt in our calculations) one obtains the same value of Δ as in SC95. However, in the radiation pressure dominated regime with $b = 1$ (as adopted e.g. by Kocsis et al. 2012a,b) the gap is wider by a factor of $\beta^{-1/3}$, making overflow less likely.

Liu & Shapiro (2010) calculated mass accretion rate across the orbit of the secondary using a local steady state model for the disk structure. They found that $\dot{M}(r_{\text{in}})$ is exponentially small when the factor⁹ in square brackets in equation (66) is large ($\gtrsim 5 - 10$). On the contrary, when this factor is $\lesssim 5$ the mass accretion rate across the orbit of the secondary is found to be close to \dot{M}_∞ . This provides justification for our use of the boundary condition $\dot{M}(r_{\text{in}}) = 0$ ($\chi = 0$) whenever $\Delta/h \gtrsim 1$, and for assuming overflow to occur for $\Delta/h \lesssim 1$.

⁸ I am grateful to Zoltan Haiman for suggesting the overflow calculations presented in this section.

⁹ Liu & Shapiro (2010) call this factor \bar{g} .

The condition (66) allows us to find the value of r at which $\Delta/h = 1$, which we call the “overflow” radius r_{of} . Assuming that when the overflow begins the disk around the binary is in the radiation pressure dominated regime (this is always the case in our calculations, see Figure 7) with $b = 0$ and h/r is given by equation (29), we find that $\Delta/h = 1$ at

$$r_{of} \approx r_{\text{Edd}} \left(\frac{\alpha}{q^2} \right)^{2/15}, \quad (67)$$

where r_{Edd} is given by equation (65).

It is clear from this expression that for equal mass binaries overflow occurs only *after* the Eddington limit becomes important since then $r_{of} \lesssim r_{\text{Edd}}$. On the other hand, as long as $q \lesssim \alpha^{1/2}$ one finds $r_{of} \gtrsim r_{\text{Edd}}$ but the actual value of r_{of} never deviates too much (i.e. not by orders of magnitude) from r_{Edd} because of the weak dependence of r_{of} on q and α . Indeed, for $\alpha = 0.1$ and $q = 10^{-2}$ one finds $r_{of} \approx 2.5r_{\text{Edd}}$.

In Figure 7 we show the position of r_{of} for each evolutionary track with open pentagons. These tags always lie close to the dot-dashed curve showing the Eddington limit (65). Another important observation that can be made by inspecting this Figure is that at least for $q > 10^{-2}$ overflow always occurs close to the start of the GW-dominated phase of the orbital evolution of the binary. Indeed, only for $q = 10^{-2}$ and only in massive disks with $\dot{M}_\infty = \dot{M}_{\text{Edd}}$ do we find that overflow *precedes* (by only a factor of ~ 2 in terms of r_b) the stage of the GW-driven evolution, see Figure 7a,c. Both for $q \sim 1$ and for $\dot{M}_\infty \ll \dot{M}_{\text{Edd}}$ (essentially irrespective of q) overflow occurs when the orbital evolution of the binary is already fully determined by the GW emission.

Kocsis et al. (2012) have derived quasi-steady solutions for the disk structure in presence of the overflow, reminiscent of the SC95 results. For these solutions to become valid after the overflow begins, information on the new boundary condition at the inner edge of the disk must propagate to the current radius of influence r_{infl} where the unperturbed, standard constant \dot{M} disk starts. Otherwise the solution would not converge to a standard constant $\dot{M} = \dot{M}_\infty$ solution at large radii and \dot{M} at the inner edge of the disk cannot be assumed equal to \dot{M}_∞ . Establishing connection to the outer disk takes of order the viscous time at r_{infl} , which is about the age of the system in our calculations. Using Figures 7 and 8 one can easily see that unless $q \lesssim 10^{-2}$ and $\dot{M}_\infty = \dot{M}_{\text{Edd}}$ the orbit of the binary evolves on a much shorter timescale than the viscous time at r_{infl} .

For example, a disk with $\dot{M}_\infty = \dot{M}_{\text{Edd}}$ around a binary with $M_c = 10^7 M_\odot$, $q = 10^{-2}$ starting at 0.01 pc begins to overflow when its period is ≈ 0.1 yr (see Figure 7a) and the orbital evolution time scale is $\approx 7 \times 10^5$ yr (Figure 8a). This is almost the same as the viscous time at r_{infl} for the corresponding evolutionary track. Thus, a quasi-steady solution can be marginally valid in this case. But if we now look at $q = 1$ binary keeping everything else the same we find overflow to occur at $P_{orb} = 0.03$ yr. At this period $t_{ev} \approx 10^3$ yr which is much shorter than the viscous time at r_{infl} ($\sim 10^7$ yr). As a result, a global quasi-steady solution does not get established in this case. Similar situation occurs for $\dot{M}_\infty \ll \dot{M}_{\text{Edd}}$ (and arbitrary q).

To summarize, the overflow across the orbit of the secondary is most important for low q , high \dot{M}_∞ systems. Even then it does not strongly affect the orbital evolution of the binary during the disk-driven stage and becomes truly important only when the binary inspiral is dominated by the GW emission. These conclusions are reached in a setup most favorable for the emergence of the overflow — radiation pressure dominated disk with ν proportional to the radiation pressure p_r . If instead ν scales with gas pressure the overflow is going to be even less important for the gas-assisted SMBH binary evolution.

5.2.7. Implications for the gravitational wave signatures of SMBH binary merger.

Our results have interesting implications for future space-based gravitational wave antennae such as LISA. If we adopt 0.03 mHz ($\approx 10^{-3} \text{ yr}^{-1}$) as a characteristic lowest frequency probed by such experiments then according to Figure 8a,b equal mass binaries with $M_c \gtrsim 10^4 M_\odot$ are detectable only when their orbital decay is already fully dominated by the GW emission, even for massive disks with $\dot{M}_\infty = \dot{M}_{\text{Edd}}$.

However, lower mass ratio systems including the so-called extreme mass ratio inspirals (EMRIs) can enter the detection band of the GW experiments during the stage when their orbital evolution is still dominated by the tidal coupling to the disk. An example of this can be seen in Figure 8b where the SMBH binaries with $q = 10^{-2}$ are pushed by the disk with $\dot{M}_\infty = \dot{M}_{\text{Edd}}$ all the way until the transition to the GW-dominated regime occurs at $P_{orb} \approx 10^{-3}$ yr. Decay of systems with even lower q or M_c can be dominated by their disks down to even shorter orbital periods, making detection of disk-driven migration quite plausible for low M_c EMRIs (provided that the strain they produce is above the signal-to-noise of the GW antenna).

Disk effects on the GW signal manifest themselves via the orbital phase shift of the binary caused by the variation of its semi-major axis due to the disk-driven migration, see Kocsis et al. (2011), Yunes et al. (2011). Even if signatures of the disk-driven migration are indeed found in the GW signal of coalescing binaries, it is unlikely that one would be able to use these measurements to probe the properties of the radiation pressure dominated part of the disk in the immediate vicinity of the binary. The reason for that again lies in the nonlocal nature of the torque acting on the binary: close to $P_{orb} = 10^{-3}$ yr evolution of all low- M_c binaries shown in Figure 7c,d is typically dominated by torques set at r_{infl} located in the *gas pressure dominated* regime. Thus, GW phase signal will contain information only about the properties of the gas pressure dominated part of the disk, and will not inform us on the physics of the inner, radiation pressure dominated regions.

We also note in this regard that the calculations of GW shifts presented in Kocsis et al. (2011) & Yunes et al. (2011) should be revised to account for this non-locality of the disk torques on the binary.

5.3. Spectra of disks around SMBH binaries.

Disks around SMBHs exhibit a set of observational signatures which distinguish them from the regular constant

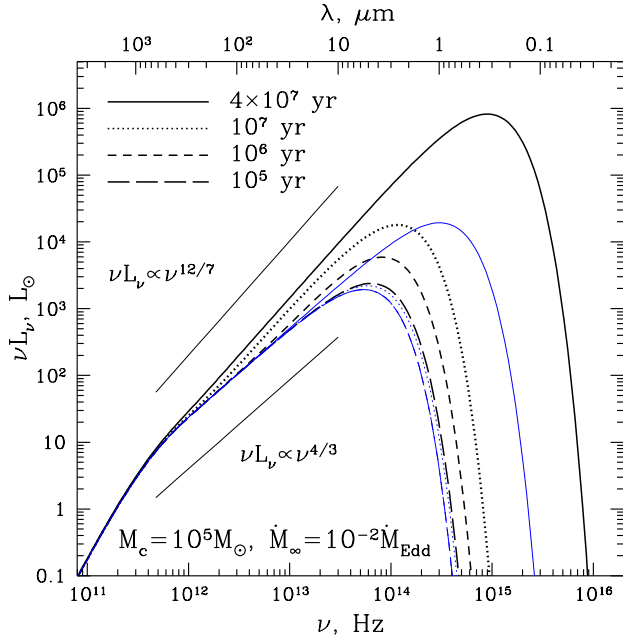


FIG. 9.— Evolution of the spectrum of a circumbinary disk evolving together with the central SMBH binary of mass $M_c = 10^5 M_\odot$ and $q = 1$, starting with initial semi-major axis 10^{-4} pc. Disk has $\dot{M}_\infty = 10^{-2} \dot{M}_{\text{Edd}}$ far from the binary and extends out to 0.1 pc. Its inner radius evolves together with the binary whose evolutionary track is shown in Figure 7d. Different curves show disk spectrum at different times labeled on the panel. Thick lines correspond to a disk self-consistently evolving under the action of the binary torque with no mass flow across the orbit of the secondary allowed ($\chi = 0$). Thin (blue) lines correspond to a constant $\dot{M} = \dot{M}_\infty$ disk occupying the same region of space. See text for details.

\dot{M} accretion disks. We illustrate this difference in Figure 9 by showing the spectral energy distribution (SED) of a circumbinary disk at different stages of the disk+binary evolution. This particular calculation assumes an equal mass, $M_c = 10^5 M_\odot$ binary starting at $r_b(0) = 10^{-4}$ pc, surrounded by a disk accreting gas at large separations at the rate $\dot{M}_\infty = 10^{-2} \dot{M}_{\text{Edd}}$; see Figure 7d for an evolutionary track of this system.

One type of spectra shown by thick curves in Figure 9 assumes radial distribution of the angular momentum flux in the disk $F_J(r, t)$ to be given by equation (64) with $r_{\text{inff}}(t)$ taken from the self-consistent calculations presented in Figure 7d. Another set of SEDs (thin curves) is computed for the same moments of time (and for the same values of $r_b(t)$) for a standard constant $\dot{M} = \dot{M}_\infty$ disk extending down to the binary orbit $r_b(t)$. In this case $F_J(r, t) = \dot{M}_\infty (GM_c r)^{1/2}$ through the entire disk. Both kinds of calculations assume an outer edge of the disk to lie at 0.1 pc (in this calculation we disregard complications arising at large separations, which are mentioned in §3.1.3.1.5; the choice of the outer radius is not important to us). We now go over the details of these calculations.

After $t = 10^5$ yr of evolution the binary semi-major axis has essentially not changed and the radius of its tidal influence has extended only out to 3×10^{-4} pc. Since this value of r_{inff} is close to r_b , binary torques affect only the very innermost part of the disk and the spectra computed

in two ways (thick and thin long-dashed curves in Figure 9) do not show significant difference. At $\lambda = 10 - 500 \mu\text{m}$ both are well fit by a power law $\nu F_\nu \propto \nu^{4/3}$ typical for a constant \dot{M} disk.

At $t = 10^6$ yr r_b is still very close to $r_b(0)$, but the effects of the binary torque have been viscously transmitted through the disk out to $r_{\text{inff}} \approx 1.7 \times 10^{-3}$ pc. This results in a factor of ≈ 4 difference in the torque acting on the binary in two cases, and noticeably changes the spectrum of the disk in a self-consistent calculation: the peak wavelength of the spectrum shifts to a slightly shorter wavelength and the peak amplitude of νF_ν increases by a factor of 2 compared to $t = 10^5$ yr. Note that the latter is a consequence only of the change in the disk structure due to binary torques — the inner disk radius stays essentially the same in these two epochs. For the same reason there is not difference in the spectra computed assuming constant \dot{M} disk (the thin curves for $t = 10^5$ and 10^6 essentially overlap in Figure 9).

At $t = 10^7$ yr r_b has shrunk to 8.7×10^{-5} pc, while $r_{\text{inff}} \approx 10^{-2}$ pc. Prior to this moment of time the disk in the immediate vicinity of the binary was in a gas pressure dominated state with free-free opacity, and the radius of influence was also in the same regime. At $t = 10^7$ yr binary starts entering the gas pressure dominated part of the disk with $\kappa = \kappa_{\text{es}}$, see Figure 7d. While the spectrum of a constant \dot{M} disk is almost the same at this epoch, the SED of a self-consistently evolved disk (thick dotted curve) exhibits not only an increase in amplitude and a shift towards shorter wavelengths, but also a change in slope at $\lambda = 10 - 500 \mu\text{m}$: in this range νF_ν is clearly steeper than $\nu^{4/3}$. All that is again predominantly due to the evolution of the radial structure of the disk under the action of the binary torque.

Finally, at $t \approx 4 \times 10^7$ yr binary orbit shrinks to 10^{-5} pc, while $r_{\text{inff}} \approx 0.03$ pc. Note that at this separation orbital evolution of the binary is dominated by the GW emission rather than the disk torques, see Figure 7d. However, the binary still causes the disk to evolve as long as its torque prevents the mass inflow into the inner cavity.

Reduction of r_b leads to a change of a constant \dot{M} disk SED — its peak is now around $1 \mu\text{m}$ (thin solid line) and the peak of νF_ν is about an order of magnitude higher than before. But the variation of the spectrum of a self-consistently evolved disk (thick solid line) is far more dramatic — it now peaks in the optical at $0.3 \mu\text{m}$ and the peak value of νF_ν is ≈ 40 times higher than for a constant \dot{M} disk. Between $1 \mu\text{m}$ and $500 \mu\text{m}$ the shape of the SED is well fit by $\nu F_\nu \propto \nu^{12/7}$, as expected for a constant F_J disk (SC95), now occupying the inner third of the radial extent of the disk and accounting for most of its luminosity.

To summarize, the SED of a disk affected by the torque of a central binary is steeper, brighter, and extends to shorter wavelengths than the SED of its constant \dot{M} counterpart having the same inner radius and mass accretion rate \dot{M}_∞ at large distances.

These features (especially the steepness of the spectrum) in principle make it possible to predict the existence of a compact central binary in a disk based on the broadband spectroscopy alone, even in the absence of

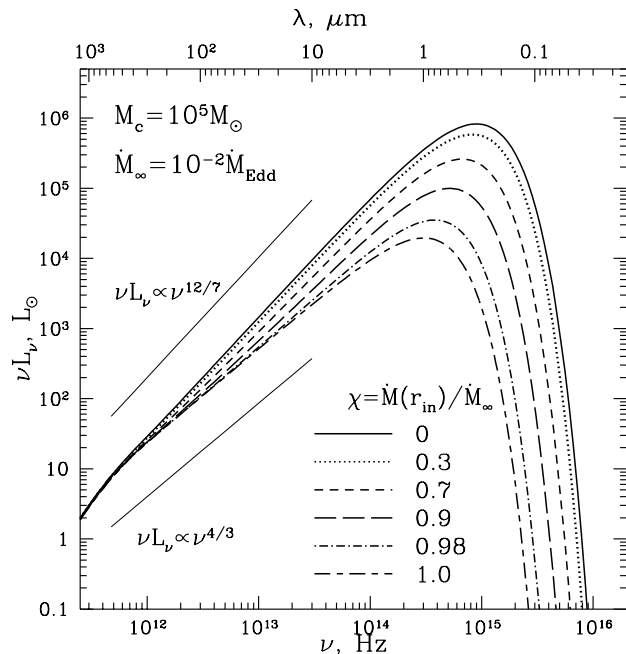


FIG. 10.— Dependence of the disk spectrum on the fraction of mass inflow $\chi = \dot{M}(r_{in})/\dot{M}_\infty$ that penetrates across the orbit of the secondary and leaves the circumbinary disk. Different curves correspond to different χ as labeled on the panel. Calculations are done for the situation depicted by solid curves in Figure 9, i.e. after 4×10^7 yr of evolution of the disk+binary system shown there.

other indications of a SMBH binary such as the double-peaked line profiles caused by the relative motion of the binary components. This method may be the only way of inferring the presence of a binary in systems with face-on orientation. Relative brightness of disks affected by the binary torque should facilitate the detection of such systems out to large distances.

5.3.1. Sensitivity of the SED to mass inflow across the secondary orbit.

So far our calculations of the SMBH binary evolution and electromagnetic signatures have explicitly assumed that the binary torques completely prevent mass inflow from the circumbinary disk across the orbit of the secondary. This allowed us to use the boundary condition $\dot{M}(r_{in}) = 0$ in all our calculations, resulting in constant F_J disk near the binary.

If the zero inflow requirement is relaxed and $\dot{M}(r_{in}) \neq 0$ then one can still construct both the steady state and the evolving self-similar solutions as demonstrated in §2.2.2 & 4.4.1. Based on these solutions one can easily extend our results for the orbital evolution of the SMBH binary presented in §5.1 & 5.2 to the case of non-zero mass inflow at the inner edge of the circumbinary disk.

Here we only show how the SED of the disk evolves as one varies the transparency of the inner barrier presented to the gas inflow by the binary torques. In Figure 10 we show disk spectra computed assuming different values of $\chi = \dot{M}(r_{in})/\dot{M}_\infty \leq 1$. Instead of equation (64) we now approximate the spatial distribution of F_J by the following simple formula:

$$F_J(r) = \begin{cases} \dot{M}_\infty l(r), & r > r_{\text{inff}}, \\ \dot{M}_\infty [l_{\text{inff}} - \chi (l_{\text{inff}} - l(r))], & r \leq r_{\text{inff}}, \end{cases} \quad (68)$$

where $l(r) = (GM_c r)^{1/2}$, $l_{\text{inff}} = (GM_c r_{\text{inff}})^{1/2}$. This prescription consists of two steady state solutions continuously matched at $r = r_{\text{inff}}$ but with different \dot{M} inside and outside of this point. For $\chi = 0$ this formula naturally reduces to equation (64).

Our calculations assume a system for which a spectrum is shown in Figure 9 at $t = 4 \times 10^7$ yr for $\dot{M}(r_{in}) = 0$, i.e. an equal mass, $M_c = 10^5 M_\odot$ SMBH binary at $r_b = 10^{-5}$ pc surrounded by a disk with $\dot{M}_\infty = 10^{-2} \dot{M}_{\text{Edd}}$, and $r_{\text{inff}} \approx 0.03$ pc. We show the spectrum of only the *circumbinary* disk, i.e. in this calculation we do not account for the emission produced by an accretion disk(s) around the primary and/or secondary which should form when mass flows across the orbit of the secondary.

One can see that as the transparency of the tidal barrier χ increases towards unity the disk spectrum steadily approaches that of a constant $\dot{M} = \dot{M}_\infty$ disk. This is not at all surprising because in the limit $\chi \rightarrow 1$ disk structure reduces to that of a constant \dot{M} disk, see Figure 3. As a result the slope of the power law portion of the spectrum steadily goes down from 12/7 to 4/3 as χ is varied from 0 to 1.

It is also clear from Figure 10 that SED is strongly affected compared to the case of a constant \dot{M} ($\chi = 1$) disk even if only a small amount of inflowing mass gets accumulated at the inner edge of the disk. For example, peak amplitude of the disk spectrum for $\chi = 0.98$ (implying that only 2% of the accreting mass gets stopped by the binary torques) is a factor of 2 higher than in the $\chi = 1$ case. And if the tidal barrier allows penetration of only 30% of the gas across the gap, the SED of the circumbinary disk is hardly distinguishable from that of a $\chi = 0$ disk with no gas inflow at r_{in} .

These results imply that the broadband SED of the disk is a rather sensitive measure of even a small amount of matter penetrating into the cavity cleared by the SMBH binary. Coupled with the measurements of the SED of the accretion disk(s), which may form around each of the binary components if $\chi \neq 0$, these observations can inform us on the efficiency of the binary torques at clearing a clean cavity at the center of the system.

6. SUMMARY.

In this work we explored the coupled evolution of a SMBH binary and a gaseous disk around it. Disk properties (surface density, temperature, etc.) evolve under the action of binary torques, which constrain the flow in the inner part of the disk. To study this problem we have re-formulated evolution equations in terms of the angular momentum flux F_J . This significantly simplifies treatment of the steady state disk structure, when F_J is a simple linear function of the specific angular momentum l .

We derived the disk properties as a function of F_J in different physical regimes that may be realized in circumbinary disks around SMBH binaries. We demonstrated that radiation pressure can limit the value of F_J in disks around massive SMBH binaries by making the disk geometrically thick and susceptible to launching a radiation-driven wind.

When the external mass supply to the disk at large distances is not matched at the inner edge of the disk because of the binary torques, the disk evolves towards es-

establishing a quasi-steady state in the inner region, where the local viscous timescale is shorter than the evolution time of the system. Viscous angular momentum flux in the inner disk steadily grows in time, which accelerates orbital evolution of the binary.

We explored the dependence of this general picture on the system parameters (mass of the binary, mass accretion rate through the disk, etc.) and found the following in agreement with previous studies.

1. Tidal coupling to a circumbinary disk can substantially (by orders of magnitude) shorten the lifetime of the binary (IPP; Lodato et al. 2009; Haiman et al. 2009).
2. For a long period before the GW emission takes over, the binary evolves in the limit when the mass of the secondary is much larger than the local disk mass (Haiman et al. 2009).
3. Disk-driven evolution of the binary can be measurable by the space based gravitational wave antennae for low q systems with relatively low M_c (Kocsis et al 2011; Yunes et al. 2011).
4. Spectrum of the disk affected by the binary torques is different from that of a conventional constant \dot{M} disk: it extends to shorter wavelengths and more power is emitted. Instead of $\nu F_\nu \propto \nu^{4/3}$ the SED of a circumbinary disk exhibits a power law segment with $\nu F_\nu \propto \nu^{12/7}$ (SC95).

We also obtain a number of new results, summarized below.

1. Self-consistent evolution of the disk resulting in a pile-up of mass at its inner edge accelerates the orbital evolution of the binary.
2. Disk-binary coupling has a non-local character: the torque acting on the binary is determined by the state of the disk far from the binary, at the radius of influence r_{infl} , which steadily increases in time,

rather than by the disk properties in the immediate vicinity of the binary.

3. Evolution of the binary orbits exhibits a phenomenon of hysteresis — dependence of the evolution on the past history of the system, which is caused by the non-locality of the disk-binary coupling.
4. Radiation pressure can strongly affect the disk structure even in cases when the mass accretion rate at large distances (in the constant \dot{M} portion of the disk) is considerably sub-Eddington.
5. Gas overflow across the orbit of the secondary affects binary mainly (or only) during the GW-dominated phase of its orbital evolution and is most important for low q , high \dot{M}_∞ systems.
6. Spectra of circumbinary disks strongly depend on the ability of accreting gas to cross the orbit of the secondary or otherwise leave the system, thus giving rise to a non-zero value of \dot{M} at the inner edge of the disk.

This list clearly implies that properly accounting for the fully self-consistent, time-dependent evolution of circumbinary disks is crucial for understanding gas-assisted SMBH mergers. This general conclusion will hopefully inspire re-evaluation of some of the existing results for the orbital evolution of SMBH binaries and their observational manifestations, both in the electromagnetic and the GW domains. Results of this work can also be extended to studying circumbinary disks around stellar mass binaries.

I am indebted to Pavel Ivanov, Bence Kocsis and Zoltan Haiman for careful reading of the manuscript, open exchange of opinions, and a number of useful suggestions. The financial support for this work is provided by the Sloan Foundation, NASA grant NNX08AH87G, and NSF grant AST-0908269.

REFERENCES

- Armitage, P. J. & Natarajan, P. 2002, *ApJ*, 567, L9
 Baruteau, C. & Masset, F. 2012, arXiv:1203.3294
 Chang, P., Strubbe, L. E., Menou, K., & Quataert, E. 2010, *MNRAS*, 407, 2007
 Cuadra, J., Armitage, P. J., Alexander, R. D., & Begelman, M. C. 2009, *MNRAS*, 393, 1423
 Filipov, L. G. 1984, *Adv. Space Res.*, 3, 305
 Goodman, J. 2003, *MNRAS*, 339, 937
 Goldreich, P. & Lynden-Bell, D. 1965, *MNRAS*, 130, 97
 Haiman, Z., Kocsis, B., & Menou, K. 2009, *ApJ*, 700, 1952
 Hirose, S., Blaes, O., & Krolik, J. H. 2009a, *ApJ*, 704, 781
 Hirose, S., Krolik, J. H., & Blaes, O. 2009b, *ApJ*, 691, 16
 Ivanov, P. B., Papaloizou, J. C. B., Polnarev, A. G. 1999, *MNRAS*, 307, 79 (IPP)
 Kocsis, B., Haiman, Z., & Loeb, A. 2012a, arXiv:1205.4714
 Kocsis, B., Haiman, Z., & Loeb, A. 2012b, arXiv:1205.5268
 Kocsis, B., Yunes, N., & Loeb, A. 2011, *Phys. Rev. D*, 84, 024032
 Lightman, A. P. & Eardley, D. M. 1974, *ApJ*, 187, L1
 Lin, D. N. C. & Papaloizou, J. 1986, *ApJ*, 309, 846
 Lin, D. N. C. & Papaloizou, J. 1996, *ARA&A*, 34, 703
 Lipunova, G. V. & Shakura, N. I. 2000, *A&A*, 356, 363
 Liu, Y. T. & Shapiro, S. L. 2010, *Phys. Rev. D*, 82, 123011
 Lodato, G., Nayakshin, S., King, A. R., & Pringle, J. E. 2009, *MNRAS*, 398, 1392
 Lynden-Bell, D. & Pringle, J. E. 1974, *MNRAS*, 168, 603 (LBP74)
 Lyubarskij, Y. E. & Shakura, N. I. 1987, *Sov. Ast. Let.*, 13, 386
 MacFadyen, A. I. & Milosavljević, M. 2008, *ApJ*, 672, 83
 Milosavljević, M. & Phinney, E. S. 2005, *ApJ*, 622, L93
 Nixon, C. J., Cossins, P. J., King, A. R., & Pringle, J. E. 2011, *MNRAS*, 412, 1591
 Novikov, I. D. & Thorne, K. S. 1973, in *Black holes*, p. 343
 Papaloizou, J. & Lin, D. N. C. 1984, *ApJ*, 285, 818
 Petrovich, C. & Rafikov, R. R. 2012, arXiv:1203.5798
 Pringle, J. E. 1991, *MNRAS*, 248, 754
 Rafikov, R. R. 2002, *ApJ*, 572, 566
 Rafikov, R. R. 2006, *ApJ*, 646, 288
 Roedig, C., Dotti, M., Sesana, A., Cuadra, J., & Colpi, M. 2011, *MNRAS*, 415, 3033
 Safronov, V. S. 1960, *Annales d’Astrophys.*, 23, 979
 Shakura, N. I. & Sunyaev, R. A. 1973, *A&A*, 24, 337
 Syer, D. & Clarke, C. J. 1995, *MNRAS*, 277, 758 (SC95)
 Toomre, A. 1964, *ApJ*, 139, 1217
 Ward, W. R. 1997, *Icarus*, 126, 261
 Yu, Q. 2002, *MNRAS*, 331, 935
 Yunes, N., Kocsis, B., Loeb, A., & Haiman, Z. 2011, *Phys. Rev. Let.*, 107, id. 171103

APPENDIX

SCALING RELATIONS FOR ARBITRARY POWER LAW OPACITY.

Here we summarize scaling relations for disk properties that result when opacity is a power law function of gas temperature T and density ρ (here taken to be represented by their midplane values):

$$\kappa = \kappa_0 \rho^{\mu_1} T^{\mu_2}. \quad (\text{A1})$$

We make two additional assumptions regarding disk properties: (1) disk is optically thick and (2) radiation pressure is negligible compared to the gas pressure (radiation pressure dominated case is described by equations (29)-(33)).

Combining equations (2), (19), (25), & (26), and $\nu = \alpha c_s^2 / \Omega$ valid in the gas pressure dominated regime one finds

$$\Sigma(r) = \left[\frac{2^{2(4+\mu_1)}}{3^{10+\mu_1-2\mu_2} \pi^{6+\mu_1-2\mu_2}} \left(\frac{\sigma}{\kappa_0} \right)^2 \left(\frac{\mu}{k} \right)^{2(4-\mu_2)} \frac{F_J^{6+\mu_1-2\mu_2}}{\alpha^{8+\mu_1-2\mu_2} (GM_c)^{1+\mu_1}} \right]^{1/\epsilon} r^{-(9-\mu_1-4\mu_2)/\epsilon}, \quad (\text{A2})$$

$$T(r) = \left[\frac{2^{-(4+\mu_1)} \kappa_0}{3^{\mu_1} \pi^{2+\mu_1}} \frac{\sigma}{\sigma} \left(\frac{\mu}{k} \right)^{(2+3\mu_1)/2} \frac{F_J^{2+\mu_1} (GM_c)^{(1+\mu_1)/2}}{\alpha^{1+\mu_1}} \right]^{2/\epsilon} r^{-(11+7\mu_1)/\epsilon}, \quad (\text{A3})$$

$$\frac{h(r)}{r} = \left[\frac{2^{-(4+\mu_1)} \kappa_0}{3^{\mu_1} \pi^{2+\mu_1}} \frac{\sigma}{\sigma} \left(\frac{k}{\mu} \right)^{4-\mu_2} \frac{F_J^{2+\mu_1}}{\alpha^{1+\mu_1} (GM_c)^{(9+2\mu_1-2\mu_2)/2}} \right]^{1/\epsilon} r^{-(1+4\mu_1+2\mu_2)/(2\epsilon)}, \quad (\text{A4})$$

where $\epsilon \equiv 10 + 3\mu_1 - 2\mu_2$.

Using these results we can derive an expression for the diffusion coefficient D_J in the form (51):

$$D_{J,0} = \frac{3}{4} \left[\frac{2^{-4-\mu_1}}{3^{\mu_1} \pi^{2+\mu_1}} \alpha^{(8+\mu_1-2\mu_2)/2} \frac{\kappa_0}{\sigma} \left(\frac{k}{\mu} \right)^{4-\mu_2} (GM_c)^{6+4\mu_1} \right]^{2/(10+3\mu_1-2\mu_2)}, \quad (\text{A5})$$

$$d = \frac{2(2+\mu_1)}{10+3\mu_1-2\mu_2}, \quad p = -\frac{12+11\mu_1+2\mu_2}{10+3\mu_1-2\mu_2}. \quad (\text{A6})$$

See Lyubarskij & Shakura (1987) for similar results.

SUMMARY OF THE DIFFUSION COEFFICIENT BEHAVIOR IN DIFFERENT REGIMES.

Here we summarize the behavior of the diffusion coefficient D_J in the power law form (51) and of the self-similar exponent n defined by equation (56) for different objects and in different regimes explored in this work (see also Lyubarskij & Shakura 1987).

In the radiation pressure dominated case (§3.3.1.3.1.1) one finds for $b = 0$

$$D_{J,0} = \frac{3}{2^4 \pi^2} \alpha \frac{\kappa_{es}^2 (GM_c)^4}{c^2}, \quad d = 2, \quad p = -7, \quad n = \frac{1}{7}. \quad (\text{B1})$$

and for $b = 1$

$$D_{J,0} = \frac{3}{4} \left[\frac{1}{2^4 \pi^2} \left(\frac{k}{\mu} \right)^4 \frac{(GM_c)^6 \kappa_{es} \alpha^4}{\sigma} \right]^{1/5}, \quad d = \frac{2}{5}, \quad p = -\frac{6}{5}, \quad n = \frac{5}{14}. \quad (\text{B2})$$

Expression (B2) also holds true for the gas pressure dominated case with $\kappa = \kappa_{es}$ (§3.3.1.3.1.2).

In the gas pressure dominated case with $\kappa = \kappa_{ff}$ (§3.3.1.3.1.3)

$$D_{J,0} = \frac{3}{4} (GM_c) \left[\frac{2^{-5} \kappa_0}{3\pi^3} \frac{\sigma}{\sigma} \left(\frac{k}{\mu} \right)^{15/2} \alpha^8 \right]^{1/10}, \quad d = \frac{3}{10}, \quad p = -\frac{4}{5}, \quad n = \frac{2}{5}. \quad (\text{B3})$$